3-2014

Competing source and loss mechanisms due to wave-particle interactions in Earth's outer radiation belt during the 30 September to 3 October 2012 geomagnetic storm

D. L. Turner
University of California - Los Angeles

V. Angelopoulos
University of California - Los Angeles

W. Li
University of California - Los Angeles

J. Bortnik
University of California - Los Angeles

B. Ni
University of California - Los Angeles

See next page for additional authors

Recommended Citation

Turner, D. L., et al. (2014), Competing source and loss mechanisms due to wave-particle interactions in Earth's outer radiation belt during the 30 September to 3 October 2012 geomagnetic storm, J. Geophys. Res. Space Physics, 119, 1960–1979, doi:10.1002/ 2014JA019770.

Authors

D. L. Turner, V. Angelopoulos, W. Li, J. Bortnik, B. Ni, Q. Ma, R. M. Thorne, S. K. Morley, M. G. Henderson, Geoffrey Reeves, M. Usanova, I. R. Mann, S. Claudepierre, J. B. Blake, D. N. Baker, Chia-Lin L. Huang, Harlan E. Spence, W. S. Kurth, C A. Kletzing, and J. V. Rodriguez

AGU PUBLICATIONS

JGR

Journal of Geophysical Research: Space Physics

RESEARCH ARTICLE
10.1002/2014JA019770

Key Points:
- WPIs compete as source and loss of relativistic outer belt electrons
- EMIC waves can cause PA- and energy-dependent loss at low L* during storms
- Chorus waves can cause local acceleration of relativistic electrons

Supporting Information:
- Readme
- AuxiliaryMaterial

Correspondence to:
D. L. Turner,
drew.lawson.turner@gmail.com

Citation:
Turner, D. L., et al. (2014), Competing source and loss mechanisms due to wave-particle interactions in Earth's outer radiation belt during the 30 September to 3 October 2012 geomagnetic storm, *J. Geophys. Res. Space Physics*, *119*, 1960–1979, doi:10.1002/2014JA019770.

Received 7 JAN 2014
Accepted 27 FEB 2014
Accepted article online 3 MAR 2014
Published online 26 MAR 2014

Competing source and loss mechanisms due to wave-particle interactions in Earth's outer radiation belt during the 30 September to 3 October 2012 geomagnetic storm

D. L. Turner[1], V. Angelopoulos[1], W. Li[2], J. Bortnik[2], B. Ni[2], Q. Ma[2], R. M. Thorne[2], S. K. Morley[3], M. G. Henderson[3], G. D. Reeves[3], M. Usanova[4], I. R. Mann[4], S. G. Claudepierre[5], J. B. Blake[5], D. N. Baker[6], C.-L. Huang[7], H. Spence[7], W. Kurth[8], C. Kletzing[8], and J. V. Rodriguez[9]

[1]Department of Earth, Planetary, and Space Sciences, University of California, Los Angeles, California, USA, [2]Department of Atmospheric and Oceanic Sciences, University of California, Los Angeles, California, USA, [3]Space Sciences and Applications, Los Alamos National Laboratory, Los Alamos, New Mexico, USA, [4]Department of Physics, University of Alberta, Edmonton, Alberta, Canada, [5]The Aerospace Corporation, El Segundo, California, USA, [6]Laboratory for Atmospheric and Space Physics, University of Colorado, Boulder, Colorado, USA, [7]Institute for the Study of Earth, Oceans, and Space, University of New Hampshire, Durham, New Hampshire, USA, [8]Department of Physics and Astronomy, University of Iowa, Iowa City, Iowa, USA, [9]CIRES, University of Colorado, Boulder, Colorado, USA

Abstract Drastic variations of Earth's outer radiation belt electrons ultimately result from various competing source, loss, and transport processes, to which wave-particle interactions are critically important. Using 15 spacecraft including NASA's Van Allen Probes, THEMIS, and SAMPEX missions and NOAA's GOES and POES constellations, we investigated the evolution of the outer belt during the strong geomagnetic storm of 30 September to 3 October 2012. This storm's main phase dropout exhibited enhanced losses to the atmosphere at $L^* < 4$, where the phase space density (PSD) of multi-MeV electrons dropped by over an order of magnitude in <4 h. Based on POES observations of precipitating >1 MeV electrons and energetic protons, SAMPEX >1 MeV electrons, and ground observations of band-limited Pc1-2 wave activity, we show that this sudden loss was consistent with pitch angle scattering by electromagnetic ion cyclotron waves in the dusk magnetic local time sector at $3 < L^* < 4$. At $4 < L^* < 5$, local acceleration was also active during the main and early recovery phases, when growing peaks in electron PSD were observed by both Van Allen Probes and THEMIS. This acceleration corresponded to the period when IMF Bz was southward, the AE index was >300 nT, and energetic electron injections and whistler-mode chorus waves were observed throughout the inner magnetosphere for >12 h. After this period, Bz turned northward, and injections, chorus activity, and enhancements in PSD ceased. Overall, the outer belt was depleted by this storm. From the unprecedented level of observations available, we show direct evidence of the competitive nature of different wave-particle interactions controlling relativistic electron fluxes in the outer radiation belt.

1. Introduction

It is now understood that various wave-particle interactions (WPI) play critical roles in many of the different source, loss, and transport processes that ultimately result in drastic variations of relativistic electron levels in Earth's outer radiation belt [e.g., *Friedel et al.*, 2002; *Millan and Thorne*, 2007; *Shprits et al.*, 2008a, 2008b; *Thorne*, 2010; *Mann et al.*, 2012]. Outer belt variability is particularly strong during geomagnetic storms [e.g., *Baker et al.*, 1998; *Reeves et al.*, 1998], when activity levels are high and the effects of source, loss, and transport mechanisms can be enhanced. However, as stated by *Reeves et al.* [2003, p. 36-1], the net effect on the outer belt electrons during storms is a "delicate and complicated balance between the effects of particle acceleration and loss." During storms and other periods of significant geomagnetic activity, various source, loss, and transport processes compete with each other, resulting in net enhancements, depletions, or relatively little change of relativistic electron flux observed at different locations throughout the outer belt, and results can vary wildly from otherwise similar events [e.g., *Reeves et al.*, 2003; *Turner et al.*, 2013; *Zhao and Li*, 2013].

To further complicate the picture, the effective levels of different source, loss, and transport processes vary in both time and space depending on the complex plasma conditions within the inner magnetosphere, which in turn are driven by variations in the solar wind and interplanetary magnetic field (IMF). Source mechanisms

that have been identified as potentially important for accelerating outer belt electrons include inward radial diffusion from some source in the plasma sheet [e.g., *Schulz and Lanzerotti*, 1974] and cyclotron-resonant WPI between ~100 s of keV electrons and whistler-mode chorus waves [e.g., *Summers et al*., 1998; *Horne and Thorne*, 1998; *Horne et al*., 2005; *Li et al*., 2007]. Losses from the system occur primarily to sinks at either Earth's atmosphere at the inner boundary of the system or the outer boundary, which is ultimately the magnetopause. Loss into the atmosphere can occur due to WPI with various waves including electromagnetic ion cyclotron (EMIC) waves [e.g., *Thorne et al*., 2006; *Miyoshi et al*., 2008; *Ukhorskiy et al*., 2010], plasmaspheric hiss [e.g., *Lyons and Thorne*, 1973; *Thorne et al*., 2013a; *Shprits et al*., 2013b], and high-latitude chorus [e.g., *Shprits et al*., 2008b]. Scattering rates by these different WPI are all dependent on electron energy, equatorial pitch angle, and magnetic latitude [e.g., *Shprits et al*., 2008b]. Loss to the outer boundary can occur due to sudden inward motion of the magnetopause or outward adiabatic expansion of drift shells, which can result in loss of electrons on newly opened drift trajectories, a process called magnetopause shadowing [e.g., *Kim et al*., 2008; *Matsumura et al*., 2011]. Magnetopause shadowing can facilitate rapid outward radial transport, which, in turn, extends losses down to much lower L-shells than are immediately affected by shadowing alone; this mechanism can explain most dropouts at $L^* > \sim 4$ [e.g., *Shprits et al*., 2006; *Turner et al*., 2012a, 2012b; *Ni et al*., 2013; *Hwang et al*., 2013]. This loss mechanism is relatively independent of particle energy, equatorial pitch angle, and species [*Turner et al*., 2014] and relies on radial transport from perturbations like ultralow frequency (ULF) waves [e.g., *Hudson et al*., 2000; *Elkington et al*., 2003; *Ukhorskiy et al*., 2009].

Here, we focus primarily on WPI between relativistic electrons and EMIC and chorus waves. EMIC waves are pulsations in the Pc1-2 (0.1–5 Hz) frequency range that are generated by unstable ion distributions in the ring current [e.g., *Cornwall*, 1965; *Anderson et al*., 1992]. Favorable conditions for wave growth include strong temperature anisotropy ($T_{perp.} > T_{par.}$) for hot ring current ions that generate the waves [e.g., *Kozyra et al*., 1984] and increased plasma density, which lowers the EMIC instability threshold causing an increase in the convective wave growth rate [e.g., *Gary and Lee*, 1994; *Gendrin*, 1975]. Based on spacecraft observations, EMIC waves occur throughout the inner magnetosphere, though they tend to occur most often on the dusk- and daysides at high L-shells during periods of medium to high AE, high positive SymH, and magnetospheric compressions [*Usanova et al*., 2012]. EMICs are thought to be important for radiation belt dynamics since they can resonate with relativistic electrons causing strong pitch angle diffusion and rapid precipitation into the atmospheric loss cone [e.g., *Thorne and Kennel*, 1971]. Typically, the resonance energy lower limit for electrons is several MeV, since electrons must overtake an EMIC wave to resonantly interact with it, but this threshold can drop to ≤ 1 MeV in regions of high plasma density, such as the plasmapause and plasmaspheric drainage plumes [*Thorne and Kennel*, 1971; *Meredith et al*., 2003a; *Summers and Thorne*, 2003; *Ukhorskiy et al*., 2010]. EMIC waves in plasmaspheric drainage plumes [e.g., *Fraser and Nguyen*, 2001; *Goldstein et al*., 2004 (on plumes); *Fraser et al*., 2005] have been proposed as an effective method of emptying the outer belt rapidly across a broad range of L-shells, which could explain flux dropout events [*Borovsky and Denton*, 2009]. However, a recent survey of EMIC waves in plasmaspheric plumes by *Usanova et al*. [2013] showed that the occurrence rates of these waves in plumes are very low (~10%). Observational evidence of relativistic electron scattering and loss by EMIC waves has proven mostly elusive, yet *Miyoshi et al*. [2008] presented evidence of just that process with spacecraft observations of precipitating electrons and ions coinciding with isolated proton aurora and EMIC wave activity observed from the ground.

Whistler-mode chorus waves are electromagnetic emissions resulting from cyclotron instabilities of energetic electrons [*Tsurutani and Smith*, 1974]. Chorus consists of discrete wave elements, typically in the range 0.1–0.8 of the electron cyclotron frequency (f_{ce}, typically ranging from ~0.1 to 10 kHz throughout the outer belt zone) [*Santolik et al*., 2003; *Li et al*., 2009] that are either rising or falling in tone [e.g., *Li et al*., 2011]. Chorus also appears as banded emissions, with upper and lower bands (which can occur either simultaneously or entirely independent of one another) separated by a gap near 0.5 f_{ce} [e.g., *Tsurutani and Smith*, 1974]. Chorus activity is dependent on geomagnetic activity, with highest occurrence rates and strongest wave amplitudes during periods of strong substorm activity, as indicated by the AE index, primarily in the dawn magnetic local time (MLT) sector [e.g., *Meredith et al*., 2001, 2003b; *Li et al*., 2009]. *Temerin et al*. [1994], *Horne and Thorne* [1998], and *Summers et al*. [1998] demonstrated how chorus waves can interact with 10 s to 100 s of keV electrons in the ring current and outer radiation belt, resulting in pitch angle and energy diffusion that could potentially accelerate electrons to MeV energy in only 1–2 days. Though chorus results in scattering of lower energy (less than a few hundred keV) electrons predominantly into the loss cone, it has been shown

[e.g., *Horne et al*., 2005] that energy diffusion can dominate over pitch angle diffusion for relativistic electrons, resulting in energization and scattering toward higher equatorial pitch angles (i.e., closer to $\alpha_{eq} = 90°$) during wave-particle interactions between chorus and these electrons. Recent observations of relativistic electrons within the outer belt indicate that this mechanism may play a dominant role in the acceleration of relativistic outer belt electrons [e.g., *Miyoshi et al*., 2003; *Green and Kivelson*, 2004; *Chen et al*., 2007; *Turner et al*., 2013; *Reeves et al*., 2013; *Thorne et al*., 2013b]. *Reeves et al*. [2013] showed that the radial profiles of relativistic electron phase space density (PSD), in adiabatic invariant coordinates, were peaked at low L*, and those peaks rose in time during a rapid outer belt enhancement event in the main phase of a storm in October 2012. *Turner et al*. [2013] studied a different storm and found the same feature, namely rising peaks of PSD for equatorially mirroring electrons in the heart of the outer belt; furthermore, they found that the peaks corresponded to the same range of L-shells where strong chorus amplitudes were also observed simultaneously.

It is important to examine PSD distributions in adiabatic invariant coordinates, since this removes adiabatic variations in flux observations, which are made for some range of energy and local pitch angle at a particular location in physical space. For example, during the main phase of a geomagnetic storm, when the magnetic field in the inner magnetosphere is reduced by the enhanced ring current, electron drift shells expand outward in physical space to conserve their third adiabatic invariant (i.e., the total magnetic flux enclosed by the drift shell, Φ, or the invariant drift shell, L*). As particles move outward to regions of lower field strength and longer magnetic field lines, their energy drops to conserve the first and second invariants, μ and K (for a detailed description of the adiabatic invariants, including the definition of the drift invariant, L*, see *Roederer* [1970]). In spacecraft observations of flux at a given energy, local pitch angle, and spatial location, such purely adiabatic motion can appear as a drastic drop in electron flux, due to the typical power law nature of electron flux versus energy distributions. Adiabatic variations may also result in large and sudden variations in a time series of flux as a function of energy, pitch angle, and location because of steep gradients in the radial and/or pitch angle distributions of electrons. However, if those flux observations are properly converted to PSD in adiabatic invariant coordinates (i.e., for any fixed μ, K, and L*), purely adiabatic variations disappear (see also *Green and Kivelson* [2004] for a detailed discussion on this). Thus, PSD distributions in adiabatic invariant coordinates are critical for disambiguating adiabatic variations from non-adiabatic variations resulting from true source, loss, and transport mechanisms.

With existing missions (Van Allen Probes, THEMIS, Cluster, GOES, POES, CubeSats, etc.) and a number of ground-based observatory networks providing regional coverage, we are now able to use multipoint observations from more than a dozen spacecraft throughout the magnetosphere and near-Earth solar wind to rigorously test many of the theories of radiation belt dynamics developed over the past several decades. Toward that goal, in this paper we take advantage of the unprecedented multipoint coverage provided by NASA's Van Allen Probes, THEMIS, and SAMPEX missions, NOAA's GOES and POES constellations, and the CARISMA network of ground magnetometers during the geomagnetic storm that started on 30 September 2012. We start with a brief introduction to the various data sets and orientation of the spacecraft orbits and locations throughout the event. We next present the observations, starting with the driving conditions in the solar wind and discuss details on the various spacecraft and ground-based observations throughout the outer belt. We then present results from a detailed analysis of the evidence of competing source and loss mechanisms resulting from different WPI in the heart of the belt during the main phase and early recovery phase. In the detailed discussion that follows, we present a hypothetical evolutionary scenario of the inner magnetosphere to explain the observations in accordance with expectations from quasi-linear diffusion theory. Finally, we present the conclusions based on our interpretation of these interesting, multipoint observations.

2. Orientation and Observations

2.1. Data Sets

For this study, we examined data from various instruments on the Van Allen Probes, THEMIS, GOES, POES, and SAMPEX spacecraft, plus solar wind observations and geomagnetic indices from the OMNI data set. OMNI solar wind data are taken from various upstream solar wind monitors and propagated to the subsolar point of the Earth. The data used here include solar wind plasma and IMF data at 1 min resolution and geomagnetic indices data at 1 h resolution available from NASA's online database, CDAWeb.

The identical-twin Van Allen Probes spacecraft, RBSP-A and -B (employing the acronym from the pre-launch mission designator: Radiation Belt Storm Probes), were launched into similar near-equatorial geosynchronous-transfer-like orbits on 30 August 2012. For Van Allen Probes data, the Relativistic Electron Proton Telescopes (REPT) [*Baker et al*., 2012] and Magnetic Electron Ion Spectrometers (MagEIS) [*Blake et al*., 2013], both instruments from the Energetic particle Composition and Thermal plasma suite (RBSP-ECT) [*Spence et al*., 2013], and the Electric and Magnetic Field Instrument Suite and Integrated Science (EMFISIS) [*Kletzing et al*., 2013] were used. Relativistic electron fluxes from 11 differential energy channels ranging from ~2 to 20 MeV and full pitch angle distributions from the REPT instruments were converted to PSD for fixed adiabatic invariants using the method outlined in *Reeves et al*. [2013] and *Morley et al*. [2013] using the *Tsyganenko and Sitnov* [2005] (TS05) model. Given the energy and pitch angle ranges observed by the REPT instruments, PSD was calculated over a range of μ from 1000 to >4000 MeV/G and K from 0.015 to 0.387 $G^{1/2}R_E$ at various L* (see all PSD data in plots in the supporting information). Magnetic field and electromagnetic wave data from the EMFISIS instrument suite were used in the calculation of the first adiabatic invariant, for examining various wave activities, and for determining the plasmapause location. MagEIS data were examined (though not presented) to determine the penetration range and effective energies of energetic particle injections during the storm.

For THEMIS data, electron fluxes from the Solid State Telescopes (SSTs) [*Angelopoulos*, 2008; *Turner et al*., 2012c] were used for this study. Relativistic electron fluxes from the SSTs' four coincidence logic channels, ranging in energy from ~330 keV to >1 MeV, were converted to PSD for fixed adiabatic invariants using the method described in *Turner et al*. [2012c]. We only included flux data from the multi-detector, coincidence logic channels, since these are unaffected by energetic proton contamination in the inner magnetosphere. We have also applied a decontamination correction for shield-penetrating electrons based on results from Geant4 particle beam simulations. For conversion to PSD, only the pitch angle bin corresponding to local pitch angle of ~90° was used, ensuring very low values of K (i.e., $K < 0.02\ G^{1/2}R_E$) since the spacecraft remain very near the magnetic equator throughout their trajectories in the outer belt. The flux data were originally at either 3 s or 3 min resolution, depending on whether the instrument was in fast or slow survey mode, but all PSD data were interpolated to 1 minute time steps, to align them with the L* calculations. Additional data from the THEMIS fluxgate magnetometers [*Auster et al*., 2008] and the wave digital fields board [*Cully et al*., 2008] were also used here for the local field strength (used for calculating μ) and examining wave activity. All THEMIS data were accessed and processed using the THEMIS Data Analysis Software tools.

From the NOAA-GOES and -POES constellations, we used the following data sets: magnetic field and proton and electron fluxes from the GOES Space Environment Monitor suite of instruments [http://www.ngdc.noaa.gov/stp/satellite/goes/documentation.html], and precipitating and trapped electron and proton fluxes from the POES Medium Energy Proton and Electron Detector (MEPED) instruments [*Evans and Greer*, 2004]. All of these data are available from NOAA's National Geophysical Data Center (NGDC). From GOES, we used magnetometer data and pitch angle resolved differential-energy particle flux from the MAGED and MAGPD instruments. We examined data from three GOES spacecraft, GOES-13, -14, and -15. GOES-13 and -15 (East and West, respectively) were operating under normal conditions during this period, while GOES-14 was operating temporarily to support NOAA operations. From POES, the MEPED instruments on each spacecraft simultaneously observe both the trapped and precipitating populations using two identical ~30° field of view instruments facing approximately parallel/anti-parallel and perpendicular to magnetic field lines throughout the outer belt latitudes [e.g., *Rodger et al*., 2010]. The data used are at a temporal resolution of 16 s, which are combined from raw counts integrated over 1 s and recorded at 2 s cadence. MEPED particle count rates were decontaminated for cross-species contamination using the method described in *Lam et al*. [2010], and we used data from six available spacecraft: NOAA-15 through -19 and METOP-02.

NASA's SAMPEX mission [*Baker et al*., 1993] was officially operational from launch in 1992 until 2004, but it continued to deliver data until November 2012, when the spacecraft re-entered Earth's atmosphere. During the period of interest, SAMPEX's high inclination, approximately circular orbit had decayed to only around 305 km altitude. Here, we examined > 500 keV electrons from the LEICA instrument [*Mason et al*., 1993] at 1 s sampling rate and > 1 MeV electron count rate data from the HILT instrument [*Klecker et al*., 1993] at 20 ms sampling rate. Data from both SAMPEX instruments are shown only in the supporting information at 6 s resolution.

Finally, we have also employed data from the CARISMA network of ground magnetometers [www.carisma.ca; *Mann et al*., 2008]. We examined stations ranging in L-shell from L = 4.06 to 6.81. CARISMA fluxgate

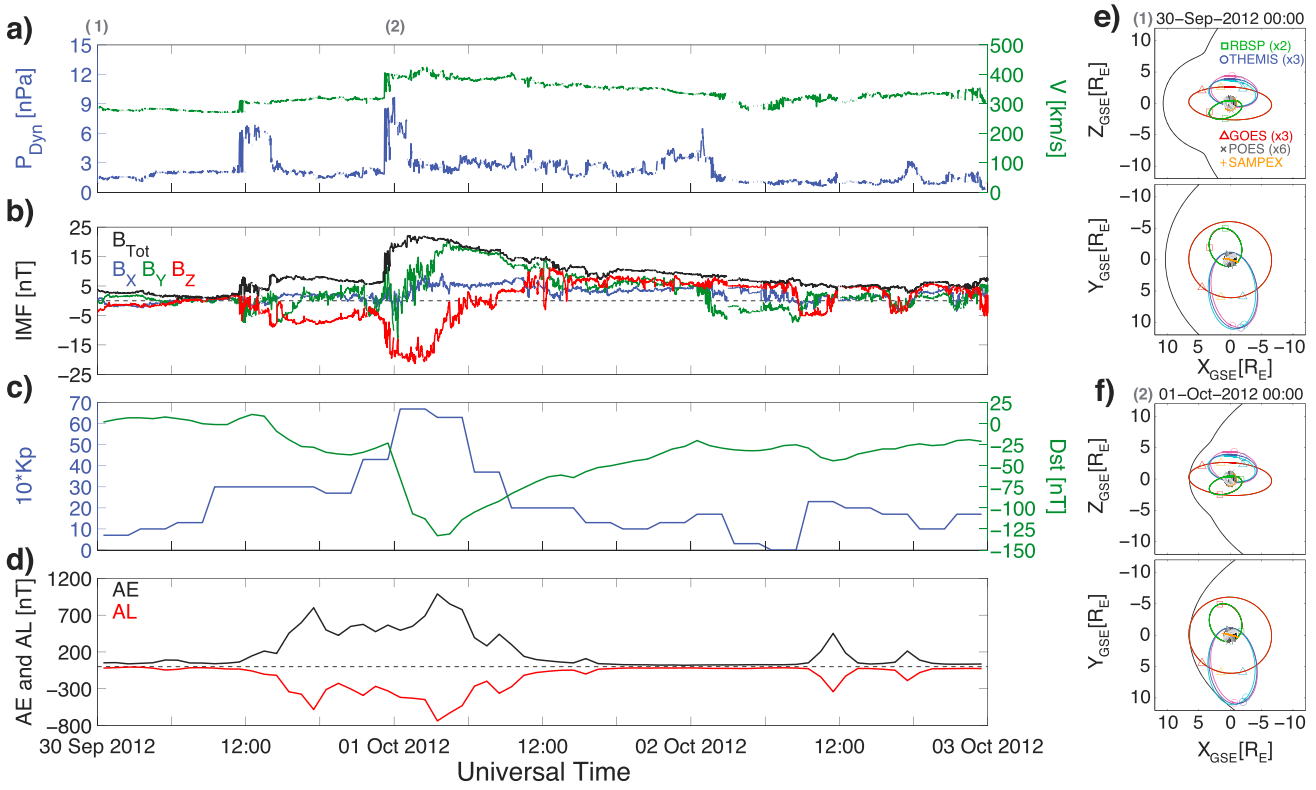

Figure 1. Solar wind and geomagnetic indices from 30 September to 3 October 2012 and spacecraft locations. (a) Solar wind dynamic pressure (P_{Dyn}, blue on the left *y* axis) and speed (V, green on the right *y* axis). (b) IMF strength (B_{Tot}, black) and components in the GSM coordinate frame (B_X, blue; B_Y, green; B_Z, red). (c) Kp index (blue, left *y* axis) and Dst index (green, right *y* axis). (d) AE (black) and AL (red) indices. (e) Van Allen Probes, THEMIS, GOES, POES, and SAMPEX orbits and spacecraft locations from 00:00 UT on 30 September. (f) The same as Figure 1e but for 00:00 UT on 1 October. For both Figures 1e and 1f, the projections of the system on the XZ_{GSE} (XY_{GSE}) plane are shown in the top (bottom) of the two plots, and the *Lin et al.* [2010] magnetopause in each plane is indicated with the black line.

magnetometer data at 8 samples/s and search-coil magnetometer data at 100 samples/s were used to calculate wave power spectral density in the EMIC frequency range (i.e., 0–1 Hz). Since EMIC waves can be ducted in the ionosphere [e.g., *Manchester*, 1966; *Neudegg et al.*, 1995; *Morley et al.*, 2009], we examined stations throughout the network and compared wave power at each. If waves were strongest at a particular station (i.e., L-shell and MLT), then we assumed that the source of the waves was nearest to there [e.g., *Mann et al.*, 2014], but if the waves showed a relatively uniform intensity over a range of stations, then we assumed that the source of the waves spanned over at least that region in space.

2.2. Solar Wind Drivers, Geomagnetic Response, and Spacecraft Orbits

A strong geomagnetic storm occurred from 30 September to 3 October 2012. Figures 1a–1d show key solar wind quantities and geomagnetic indices from this period. The storm was driven by two sudden enhancements of solar wind dynamic pressure (P_{Dyn}) and weak enhancements of solar wind speed (V) and accompanying strong southward IMF (shown in Figures 1a and 1b). Based on these observations, this was most likely a coronal mass ejection (CME)-driven event, where the magnetic cloud was observed between ~23:00 UT on 30 September and ~08:00 UT on 2 October. This solar wind activity was apparently very geo-effective. The resulting geomagnetic storm reached a Dst minimum of around -130 nT, and the Kp index reached 6.7 (Figure 1c). There was also prolonged, strong substorm activity, as indicated by the AE and AL indices (Figure 1d), during the period of southward IMF from ~11:00 UT on 30 September to ~08:00 on 1 October, corresponding approximately with the main phase of the storm. Like many CME-driven storms, the recovery phase was relatively short [*Gonzalez et al.*, 1999]. Note, too, that there was very little substorm activity during the storm recovery phase, which is consistent with the IMF remaining northward throughout the majority of that period.

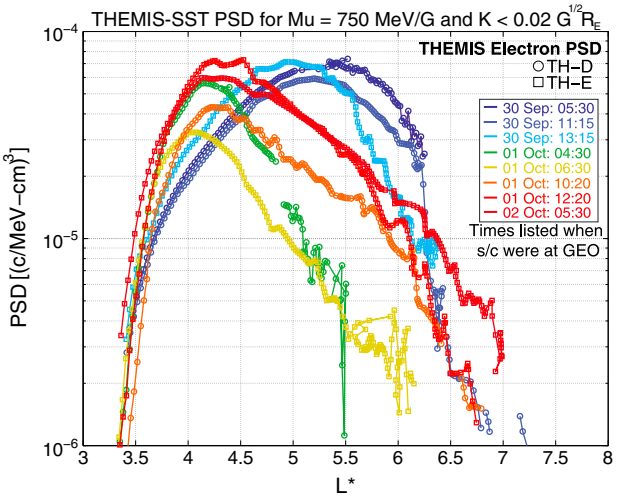

Figure 2. Relativistic electron phase space density (PSD) distributions in L* during the course of the storm as observed by THEMIS. PSDs are shown for fixed first and second adiabatic invariants, $\mu = 750$ MeV/G and $K < 0.02\,G^{1/2}R_E$, corresponding to equatorially mirroring relativistic electrons at energies of 100 s of keV to >1 MeV in the outer belt. PSD from both THD (circles) and THE (squares) are shown. Different colors correspond to different spacecraft passes through the outer belt, with the times when the spacecraft was at GEO for each distribution indicated on the legend.

Figure 1 also shows the orbits of the spacecraft used for this study in the GSE coordinate frame. The *Lin et al.* [2010] magnetopause is also included at both times shown; it was calculated for each time using the OMNI solar wind and indices data from those times. During the peak of the second solar wind pressure enhancement, the magnetopause moved in to approximately geosynchronous orbit (GEO) at the subsolar point (Figure 1f). Of the spacecraft used for this study, the two Van Allen Probes satellites were in their near-equatorial, GEO-transfer-like orbits and passed through the outer belt throughout the MLT range from pre-dawn to pre-noon. The three THEMIS spacecraft were in their near-equatorial, highly elliptical orbits with apogees located very near dusk MLT. The spacecraft were only separated along their very similar orbits by a few hours in UT. They passed through the outer belt in the mid-afternoon (i.e., around 15:00) and mid-evening (i.e., around 21:00) MLT sectors. Three GOES spacecraft, GOES-13, -14, and -15, were at GEO, i.e., ~6.6 R_E nearly circular orbits. The six POES spacecraft plus SAMPEX were all in their various low-Earth orbits (LEO), which, combined, spanned almost the full 24 h range in MLT.

2.3. Outer Radiation Belt Response to the Storm

The evolution of relativistic electron PSD for $\mu = 750$ MeV/G (i.e., ~1.2 MeV in the heart of the outer belt), $K < 0.02\,G^{1/2}R_E$ (i.e., ~75° < α_{eq} < ~105°, where α_{eq} is the equatorial pitch angle) throughout the storm is shown in Figure 2. For approximate conversions between μ, K, and E, α_{eq} for L-shells throughout the belt, please refer to the supporting information for plots of corresponding energies and equatorial pitch angles for fixed first and second adiabatic invariants in a dipole field. The different PSD distributions in L* show different orbit passes from THD and THE in different colors. The pre-storm distribution, shown in dark blue for 05:30 UT on 30 September, revealed a broadly peaked outer belt population, with a peak in PSD around L* ~5.5. As detailed in a companion paper [e.g., *Turner et al.*, 2014], the outer belt dropout event that accompanied the main phase of this storm started after 11:00 UT at higher L* and moved in over time. This corresponds well to the first sudden pressure enhancement in the solar wind, and *Turner et al.* [2014], based on observations, and *Hudson et al.* [2014], based on simulations, both concluded that at L* > 4, this dropout was entirely consistent with losses by magnetopause shadowing and subsequent rapid outward radial transport [e.g., *Shprits et al.*, 2006; *Loto'aniu et al.*, 2010; *Morley et al.*, 2010; *Kim et al.*, 2011; *Turner et al.*, 2012b]. The full extent of the dropout as observed by THEMIS resulted in the distribution shown in yellow from around 06:30 UT on 1 October.

During the late main phase and early recovery phase, THEMIS also revealed evidence of local acceleration in the form of growing peaks in PSD for fixed adiabatic invariants. This is evident in Figure 2 from the time history of the L* distributions from 06:30 to 12:20 UT on 1 October (i.e., gold, orange, and red curves in Figure 2). The peak was located at L* ~ 4 after the dropout, and over the next several hours, the PSD more than doubled between ~4.0 < L* < ~5.5 (i.e., *at least* L* of 5.5, since that was outside of range at 06:30 UT). Also, the peak moved outward and broadened throughout this period, from L* ~ 4 to L* ~ 4.2–4.5. Then, between 12:20 UT on 1 October and 05:30 on 2 October, the peak magnitude decreased between ~3.8 < L* < ~5.0 and increased at lower and higher L*s. This indicates that the local source of PSD slowed significantly or turned off and the distribution spread away from the PSD peak in L*, most likely via radial diffusion.

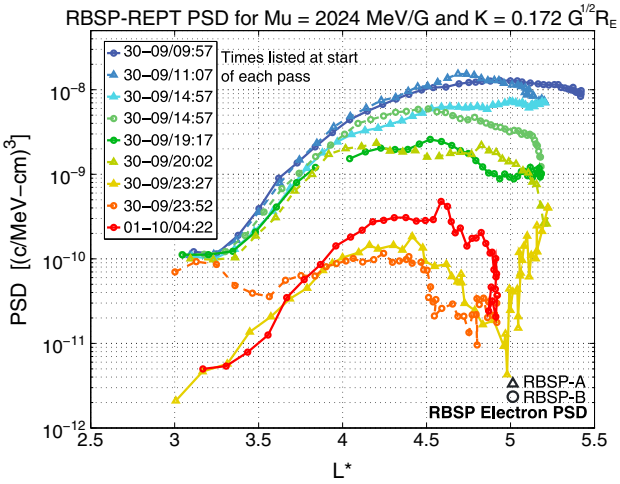

Figure 3. Relativistic electron PSD distributions in L* during the course of the storm as observed by Van Allen Probes. PSDs are shown for fixed first and second adiabatic invariants, $\mu = 2024$ MeV/G and $K = 0.172\,G^{1/2}R_E$, corresponding to off-equatorially mirroring relativistic electrons at energies of several MeV in the outer belt. PSD from both RBSP-A (triangles) and -B (circles) are shown. Different colors correspond to different spacecraft passes through the outer belt, with the start times for each distribution indicated on the legend. Inbound passes are shown with solid lines, and outbound are shown with dashed lines.

The THEMIS-SST data revealed the evolution of relativistic outer belt electrons at energies from 100 s of keV up to a few MeV out to the last closed drift shell and beyond, but RBSP-ECT REPT observed the evolution with better energy resolution at higher energies (multi-MeV) within the heart of the outer belt ($L^* \leq \sim 5.5$), which revealed significant energy and equatorial pitch angle dependencies. Figure 3 shows PSD distributions as a function of L* for $\mu = 2024$ MeV/G and $K = 0.172\,G^{1/2}R_E$ calculated from REPT fluxes. These distributions are typical for the high-μ and -K electron response to the storm main phase as observed by REPT. As detailed in *Turner et al.* [2014] and consistent with the THEMIS observations (Figure 2), the dropout started at higher L* and moved inward, and there was a sharp cutoff in the distribution at $L^* \sim 5$ around 23:30 UT. We do not focus on those features here; instead, we are concerned with the sudden loss at $L^* < 4$ between ~22:00 and 05:00 UT and the formation of a peak in PSD around $4 < L^* < 5$.

Starting with the outbound RBSP-A pass through the outer belt, shown with the dashed light green line marked 20:02 in Figure 3, the spacecraft observed some loss from the pre-event distribution at $L^* < 4$, but this loss was less than ~50%. RBSP-B's inbound pass (solid dark green line), which actually passed through $L^* < 4$ after RBSP-A had already traversed that range (compare also with the L* vs. time plot shown in the supporting information), revealed that no further loss occurred there until at least 22:30 UT. Then, on the RBSP-B outbound trajectory starting at 23:52 (orange curve), drastic losses were observed at $L^* > 3.25$. The PSD at those low L*s dropped by more than an order of magnitude in the < 3 h revisit time between the consecutive RBSP-A and -B passes. This loss continued further at $L^* < 4$ as observed by RBSP-A on its inbound trajectory that started at 23:27 UT (gold curve). By the time it got to $L^* < 4$, between 1 and 3 h after RBSP-B passed through on its outbound trajectory, the PSD at $L^* < 3.75$ revealed dramatic losses, with the loss being strongest at $3 < L^* < 3.5$, where it fell by over an order of magnitude in only ~3 h. Interestingly, THEMIS did not reveal such losses, which indicates some μ- and/or K-dependence of the loss mechanism. This was confirmed when we examined Van Allen Probes data at lower μ and K (a more detailed discussion to follow). *Turner et al.* [2014] included these sudden and drastic losses at $L^* < 4$ in their quantification of the dropout's effect and speculated that they resulted from WPI, since they were inconsistent with losses by magnetopause shadowing and subsequent rapid outward radial transport. However, they performed no thorough analysis to prove or refute that statement. We conduct such an analysis here.

The Van Allen Probes observations shown in Figure 3 also reveal additional evidence of a local source around $4 < L^* < 5$. Again, comparing the RBSP-A inbound pass starting at 23:27 UT with the RBSP-B outbound pass starting at 23:52 UT, the two spacecraft were at the same L* very near $L^* \sim 4.5$ at ~02:30 UT. The high quality of the calibrations on the REPT instruments is immediately clear considering the nearly equal quantities of PSD observed by both during this conjunction in adiabatic invariant coordinates [see also *Morley et al.*, 2013]. So, taking their respective trajectories into account during these two passes, RBSP-B observed the distributions at $L^* < 4.5$ *before* RBSP-A did. Meanwhile, RBSP-A observed the distributions at $L^* > 4.5$ *before* RBSP-B did. This shows the loss at $L^* < \sim 4$ discussed in the previous paragraph, but it also shows that at $\sim 4 < L^* < 4.5$, the PSD actually increased by up to a factor of 2 in the < 1.5 h between when RBSP-A and -B passed through that region. Meanwhile, at $L^* > 5$, the PSD continued to decrease rapidly until around the time that RBSP-B reached

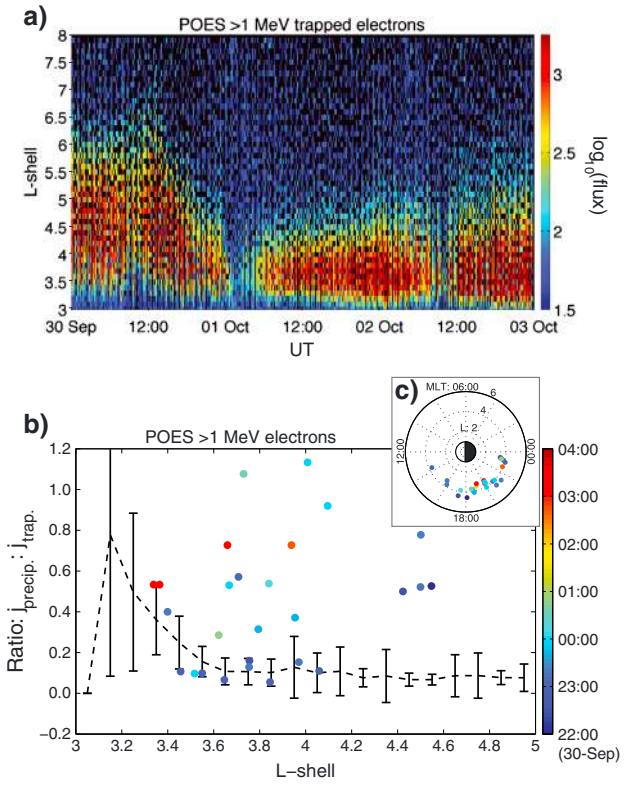

Figure 4. (a) POES >1 MeV trapped electrons binned and averaged by L-shell ($\Delta L = 0.1$) and time ($\Delta t = 15$ min). The logarithm of electron flux (units, #/cm^2-s-sr) is shown in color for 30 September to 3 October 2012. (b) POES >1 MeV precipitating to trapped flux ratios. Using all six available POES spacecraft, ratios are calculated when both the trapped and precipitating channels are above background levels when the spacecraft were in the MLT range 12:00 – 24:00 during the period of interest, 22:00 UT on 30 September to 04:00 UT on 1 October. Ratios are plotted as a function of L-shell and color coded by time of the observation during the period. The dashed black line with error bars is the pre-event (00:00 UT on 28 September to 11:00 UT on 30 September) average ratio from the same MLT range. (c) The L-MLT distribution of the observations shown in Figure 4b; each point is color coded the same as it was in Figure 4b.

apogee. At that point, around the start of its inbound trajectory starting at 04:22 UT (i.e., solid dark red curve; see also L* vs. time plot in supporting information), RBSP-B observed a very sudden increase in PSD. The PSD continued to increase on subsequent passes (not shown in Figure 3; see Figure 7 or supporting information). These observations, combined with the concurrent THEMIS observations that showed negative gradients of relativistic electron PSD beyond the Van Allen Probes apogees (e.g., green curve in Figure 2), revealed that the increase in PSD caused a growing local peak in L*, which is a clear indicator of local acceleration [e.g., *Reeves et al.*, 2013; *Thorne et al.*, 2013b]. Thus, during this storm main phase at $L^* < 5$, the combined THEMIS and Van Allen Probes observations showed that there were competing source and loss mechanisms active in the heart of the outer radiation belt. In the next section, we analyze those mechanisms in detail using these and additional observations to determine the nature and net effects of each mechanism.

3. Analysis

3.1. Relativistic Electron Loss

To develop a more comprehensive picture of what may have caused the sudden loss observed in the high-μ, high-K electrons by Van Allen Probes, we complemented the Van Allen Probes and THEMIS observations with those of >1 MeV trapped and precipitating electrons from six POES spacecraft (including the METOP-02 satellite) and SAMPEX, plus ground magnetometer data from the CARISMA network [*Mann et al.*, 2008]. Figure 4 provides a summary of the POES >1 MeV electron fluxes throughout the storm period (Figure 4a) and during the period of interest for the loss at $L^* < 4$ (Figures 4b and 4c). From the trapped flux map in Figure 4a, it is clear that the dropout started after ~12:00 UT on 30 September at higher L-shells and propagated inward in time. Then, around ~23:00 UT when the second sudden solar wind pressure enhancement impacted the system, the loss extended rapidly below $L \sim 4.5$ and within only a couple of hours engulfed the entire outer belt population, bringing the POES trapped fluxes to background levels throughout the full range of outer belt L-shells.

Focusing on the period from 22:00 UT on 30 September to 04:00 UT on 1 October, we examined the POES fluxes from different L-shells, latitudes, and MLTs and found that there were very strong precipitating fluxes (above background and pre-event average levels) at low L-shells in both hemispheres in the dusk-to-midnight MLT sector during this period. To demonstrate this, Figure 4b shows the ratios of precipitating to trapped fluxes observed by all six POES spacecraft over the L-shell range $3 < L < 6$, between noon and midnight MLT in both hemispheres between 22:00 and 04:00 UT. The precipitation was bursty, with sudden increases in the precipitation fluxes observed for only a few time steps out of the typical background levels, which were not included for the ratio calculations. Most of the strong precipitation occurred during the

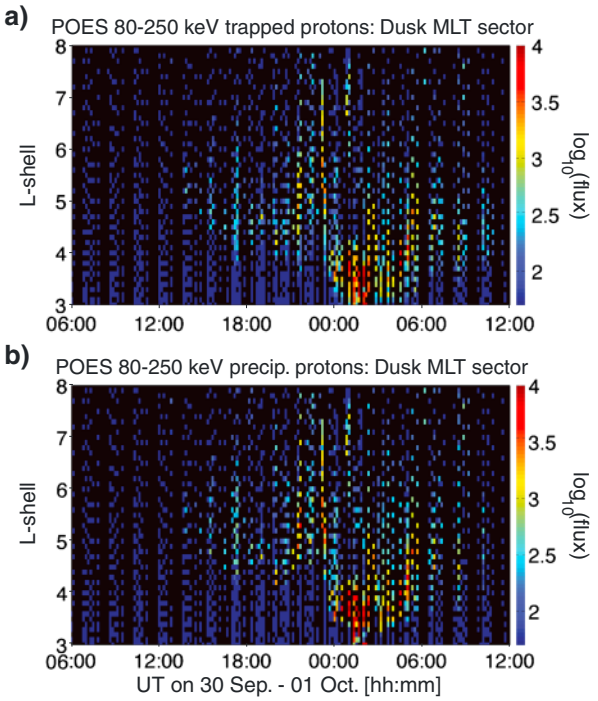

Figure 5. (a) POES trapped and (b) precipitating protons from the 80 to 250 keV channel. The logarithm of proton flux (units, #/cm^2-s-sr-keV) is shown in color for $3 \le L \le 8$ from 06:00 UT on 30 September to 12:00 UT on 1 October 2012. Fluxes have been binned and averaged by L-shell ($\Delta L = 0.1$) and time ($\Delta t = 15$ min) when each POES spacecraft was in the dusk MLT sector (15:00 – 21:00 MLT) only.

beginning of this period, and it is clear from the average trapped distribution that there was significant loss of the trapped population observed from LEO, consistent with the observations from Van Allen Probes at higher altitudes closer to the equator. The precipitating fluxes, which represent electrons deep within the atmospheric loss cone, revealed significant precipitation through this period, with several observations at the strong diffusion limit (ratio ~ 1). Typically, these >1 MeV precipitating electrons are at the instrument background level (i.e., at or below the 1-count level). Excluding the slot region (L < ~3.5, where both trapped and precipitating fluxes are typically around background levels), the pre-event average ratio included precipitating fluxes near (but just above) the background level of the instruments, which when combined with the pre-storm trapped distribution yielded the average pre-event ratio of ~10–20%. We confirmed that throughout this storm, 22:00 UT on 30 September to 04:00 UT on 1 October was the only period when there was any significant precipitation of this energy electrons observed by POES spacecraft. The precipitating fluxes peaked between 23:00 and 01:00 UT, at ~18:00 to ~22:00 in MLT, $3.5 < L < 4.5$ (see Figure 4c; $3.5 < L < 4.5$ corresponds approximately to $3.2 < L^* < 4.0$), and approximately the same levels in both the northern and southern hemispheres based on near-simultaneous observations from multiple spacecraft.

SAMPEX also revealed enhanced levels of relativistic electrons at LEO during this period (not shown here; see plots of >500 keV and >1 MeV count rates in the supporting information). From the passes through the outer belt between 18:00 and 02:00 UT, it is clear that in the dusk MLT sector (~19:00 MLT) at L < 4, the count rates of >1 MeV electrons increased by almost an order of magnitude at 22:50 and 00:20 UT compared to the passes through the same L and MLT before (18:20 UT) and after (01:50 UT). Most interestingly, and providing further evidence of the energy dependence of this loss, the >500 keV count rates from SAMPEX did not show a similar increase, except at very low L-shells (L < ~3.5) later in the period.

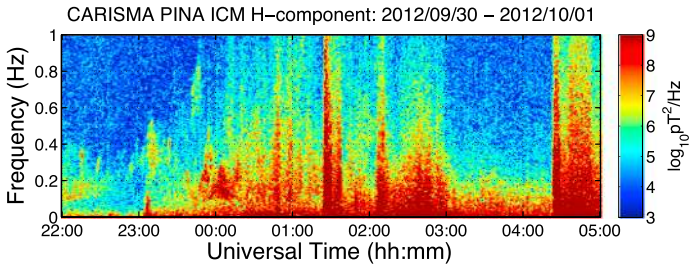

Figure 6. Fourier spectrogram of wave data from the CARISMA ground magnetometer station at Pinawa (L = 4). Data from the H-component are shown for 22:00 UT on 30 September to 05:00 UT on 1 October 2012 in the EMIC frequency range (0–1 Hz). The corresponding MLT at Pinawa over this range in UT was from 15:24 to 22:24 MLT.

Strong precipitation of >1 MeV relativistic electrons into the dusk MLT atmosphere is suggestive of rapid scattering by EMIC waves. These waves are excited by anisotropic pitch angle distributions of ions and result in scattering losses of energetic protons. Fortunately, POES-MEPED instruments also observe trapped and precipitating protons with energies from 10 s of keV to several MeV. Figure 5 shows

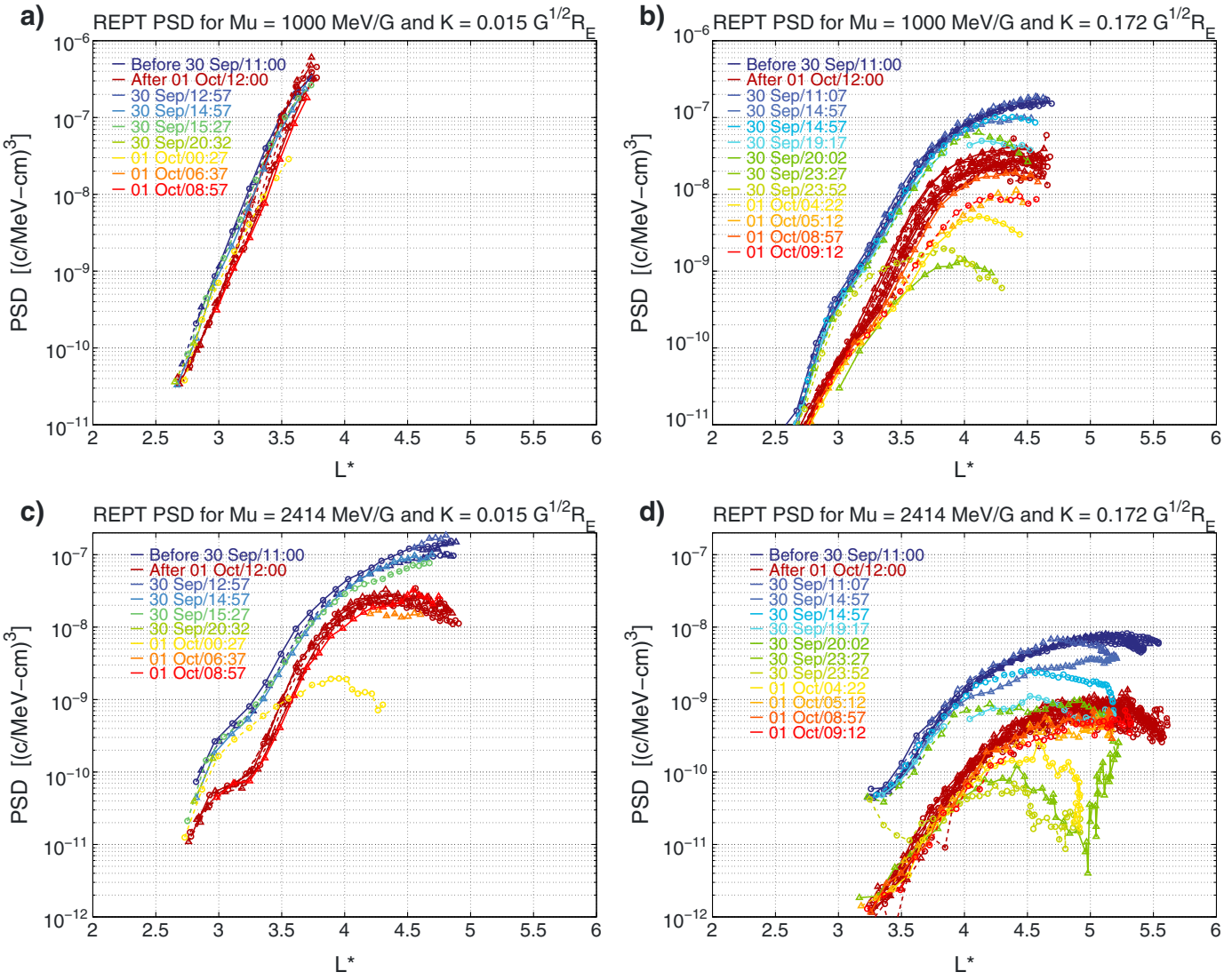

Figure 7. Relativistic electron PSD distributions as a function of L* for different μ and K during the course of the storm as observed by Van Allen Probes. PSDs are shown in the same format as Figures 2 and 3 for fixed values of the first and second adiabatic invariants: (a) $\mu = 1000$ MeV/G, $K = 0.015\ G^{1/2}R_E$; (b) $\mu = 1000$ MeV/G, $K = 0.172\ G^{1/2}R_E$; (c) $\mu = 2414$ MeV/G, $K = 0.015\ G^{1/2}R_E$; (d) $\mu = 2414$ MeV/G, $K = 0.172\ G^{1/2}R_E$. All distributions from before 11:00 UT on 30 September are shown in dark blue, while all those from after 12:00 UT on 1 October are shown in dark red. The other colors correspond to distributions from passes between those two times, and the start times for each are indicated in the corresponding legends.

trapped and precipitating flux maps of 80–250 keV protons in the dusk MLT sector (15:00 – 21:00 MLT) during the pre-storm and storm main phases. Before the storm started, the POES spacecraft only observed background flux levels throughout the range of L-shells shown, but enhancements in both the trapped and precipitating populations started within a few hours of the storm sudden commencement associated with the first sudden solar wind pressure enhancement on 30 September After ~23:00 UT and the impact of the second solar wind pressure enhancement, the trapped and precipitating fluxes of protons became more enhanced and stayed elevated until ~06:00 UT. Interestingly, the enhancements were mostly limited to $3 < L < 4.5$, other than signatures of precipitation that span a broad range in L but only last briefly in time, which we interpret as energetic particle injections from the plasma sheet. Since the flux levels of precipitating protons were at the same level as the trapped proton fluxes, the losses to the atmosphere were at the strong diffusion limit; this is another strong indicator of EMIC wave activity at these L-shell and MLT ranges during this period.

Finally, we also looked for direct observations of EMIC waves from THEMIS, Van Allen Probes, and the CARISMA network of ground magnetometers. Unfortunately, the three THEMIS spacecraft were all near apogee during

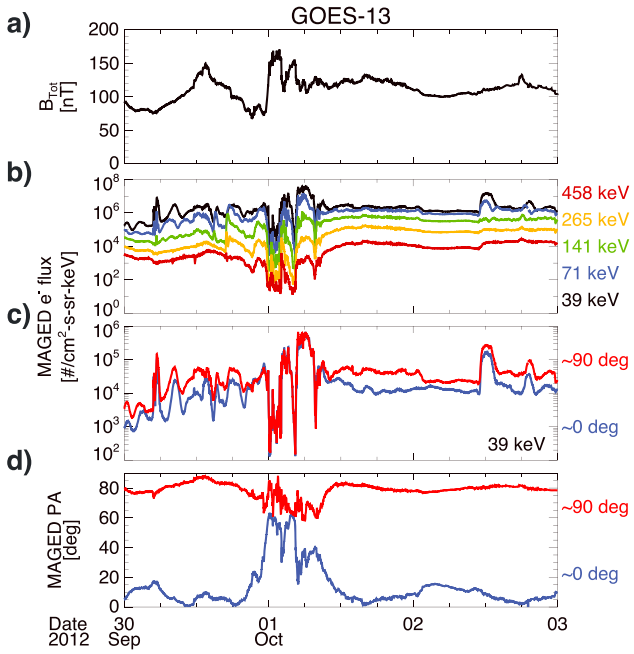

Figure 8. Data from GOES-13 during the event. (a) Magnetic field strength. (b) Omnidirectional differential electron fluxes from the MAGED data, with different colors corresponding to different energies, as labeled on the right of the plot (channel equivalent energies are calculated as the square root of the product of the upper and lower energy thresholds for each channel). (c) 39 keV electron flux from the MAGED telescopes nearest to local pitch angles of 90° (red) and 0° (blue), with the actual measured pitch angle for each telescope shown in Figure 8.

the period of interest (i.e., 22:00 – 02:00 UT). However, when they did pass through these low L-shells both before and after the sudden loss occurred at $L^* < 4$, THEMIS did not observe any EMIC wave activity, indicating that if EMIC waves were present during the period of interest then they did not last for more than ~9 h. The Van Allen Probes also revealed no EMIC waves along their orbits during the period and ranges of interest. However, both Van Allen Probes spacecraft were in the dawn MLT sector, revealing that there were no EMIC waves on that side of the system, which is also of interest considering the lack of >1 MeV precipitation observed there (not shown). The CARISMA network in North America, however, does span the L-shells of interest (i.e., $3 < L < 5$) and, most fortunately, North America was in the dusk MLT sector around 00:00 UT on 1 October. Figure 6 shows wave power spectral density from the Pinawa station located at $L = 4$. The range in UT on this plot corresponds to 15:24 to 22:24 MLT at the station. At Pinawa, band-limited Pc1-2 emissions (consistent with EMIC waves) were observed starting around 22:00 UT and lasting until around 01:30 UT, when broadband wave activity dominated the frequency spectrum. The EMIC waves revealed structured forms prior to ~23:45 UT and, from then until 01:30 UT, a broader band of more powerful, nearly continuous wave activity with peak power around ~0.2 Hz but extending also to higher frequencies. After the broadband wave activity subsided around 03:00 UT, there was no longer any evidence of EMIC waves from this station. Based on comparisons with other stations, the EMIC waves observed from 22:00 to 01:30 UT were limited to $3 < L < 5$.

When the electron PSDs from REPT were examined for a broad range of μ and K, as shown in Figure 7, there was clear evidence of a significant μ- and K-dependence on the magnitude of the loss at $L^* < 4$. The evolution of the PSD distributions in L^* for $\mu = 2414$ MeV/G and $K = 0.172\ G^{1/2}R_E$ (Figure 7d) was very similar, both qualitatively and quantitatively, to that shown for $\mu = 2024$ MeV/G and $K = 0.172\ G^{1/2}R_E$ in Figure 3. Throughout the L^* range that could be observed at this μ and K from REPT, the PSD dropped by at least an order of magnitude between the distributions observed around 23:27 and 04:22 UT. However, for the same μ but $K = 0.015\ G^{1/2}R_E$ (Figure 7c), the loss at $L^* < 4$ was not as severe. For example, at $L^* \sim 3.5$, the loss was only around a factor of 2 between 00:27 and 06:37 UT, while at $L^* \sim 3$, the loss was closer to a factor of 4 over the same period. Throughout the range $L^* < 3.5$, the loss was most extreme at $L^* \sim 3.2$. Next, examining lower-μ electrons, the loss was again much stronger for higher-K PSD (e.g., $\mu = 1000$ MeV/G, $K = 0.172\ G^{1/2}R_E$ in Figure 7b). For lower-K (e.g., $\mu = 1000$ MeV/G, $K = 0.015\ G^{1/2}R_E$ in Figure 7a), the loss was only between a factor of 2 and 4 with the strongest loss occurring at higher L^*. However, this entire picture is complicated by the evidence of a source of PSD occurring simultaneous with the loss.

3.2. Relativistic Electron Source

From Figures 2, 3, and 7, it is evident that some source of PSD resulted in a growing peak of PSD around $3.5 < L^* < 5$ during the early hours (UT) of 1 October. After ~12:00 UT on 1 October, however, the peak

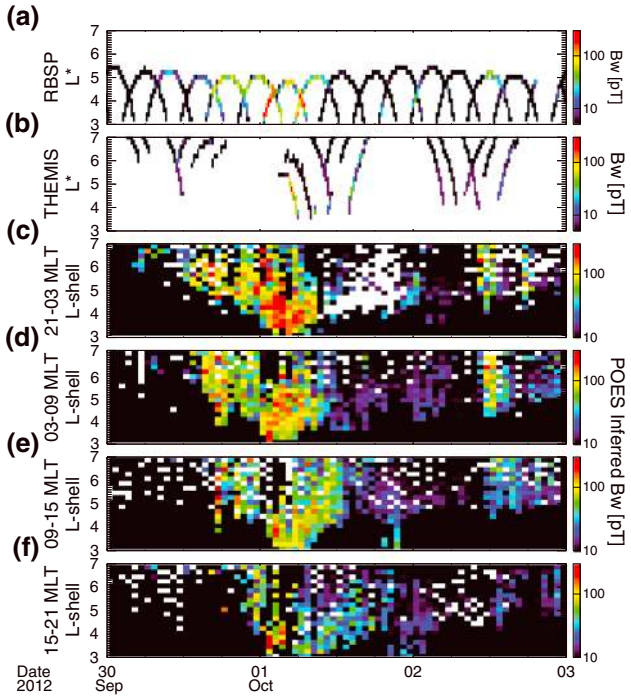

Figure 9. Chorus wave amplitudes (Bw, in color), sorted by UT from 30 September to 3 October and L* for (a) RBSP and (b) THEMIS. For Van Allen Probes, wave amplitudes were calculated by integrating magnetic wave power spectral density over 0.1–0.8 f_{ce} and for THEMIS RMS wave amplitudes of FBK data were calculated over 0.1–0.8 f_{ce}, where f_{ce} is the electron cyclotron frequency. Figures 9c–9f show estimated chorus wave amplitudes (in color) as a function of UT and L-shell inferred from the POES precipitating vs. trapped flux ratio of 30–100 keV electrons. Figures 9c, 9d, 9e, and 9f correspond to results from the midnight, dawn, noon, and dusk MLT sectors, respectively.

stopped growing, indicating that the source of PSD energization ceased or was approximately balanced by any ongoing losses or transport away from the peak in PSD. Based on THEMIS PSDs (Figure 2), the peak level of PSD for low-μ, low-K electrons increased by at least a factor of ~4 between around 06:30 and 12:20 UT on 1 October. As observed by the Van Allen Probes (Figure 7b), the peak level of PSD increased by a factor of >10 between 00:00 and 12:00 UT. At higher μ, the peak in PSD increased by a factor of ~15 in around 9 h for $K = 0.015\,G^{1/2}R_E$ (Figure 7c), and by a factor of ~8 over the same period for $K = 0.172\,G^{1/2}R_E$ (Figure 7d). THEMIS observed peaked PSD distributions in L* throughout the storm, consistent with the Van Allen Probes observations at higher μ and K.

Multiple energetic particle injections were observed throughout the inner magnetosphere by THEMIS, Van Allen Probes (not shown here), and GOES, as shown in Figure 8. Before the storm sudden commencement, GOES-13 observed an energetic particle injection at ~05:00 UT; the upper energy threshold on this injection was ~141 keV. The frequency of injection events was highest during the main phase of the storm (i.e., between ~13:00 UT on 30 September and ~04:00 UT on 1 October). During the main phase of the storm, injections were observed at ~15:00, ~17:00, and ~21:00 UT, with the energy threshold increasing up to at least 458 keV by the last of these. Using observations from all three GOES spacecraft, we determined whether the strong variations observed in the fluxes and magnetic field strength between ~00:00 and ~09:00 UT were more consistent with localized energetic particle injections or more global reconfigurations of the magnetic field topology itself. Such large-scale reconfigurations can result in the GOES spacecraft crossing from the trapping region to open drift shells that connect to the magnetopause or the lobes. Based on multi-spacecraft analysis, there were at least a dozen more energetic particle injections during the main phase, including the two largest variations around 02:00 and 04:30 UT. Proton injections were also observed in the GOES-MAGPD instruments throughout the main phase (see supporting information). These GOES observations are also consistent with the AL index (Figure 1) and the Van Allen Probes and THEMIS flux observations during this period, which also revealed multiple particle injections during the main phase. Injection activity died down after ~12:00 UT on 1 October, with only two isolated injections being observed around 11:00 and 18:00 UT on 2 October. Note that spikes in the AL index accompanied both of those last injections.

With THEMIS, Van Allen Probes, and POES, we also examined the chorus wave activity during this storm. Figure 9 shows chorus wave amplitudes observed by Van Allen Probes (Figure 9a) and THEMIS (Figure 9b) and derived from POES 30–100 keV electron flux observations as described in *Li et al.* [2013] (Figures 9c–9f). Recall that the Van Allen Probes spacecraft were in the dawn-to-noon MLT sector, THEMIS spacecraft were in the dusk sector, and POES can be used for the full range in MLT. Based on comparing the observations from Van Allen Probes and THEMIS, chorus wave amplitudes were stronger in the dawn

sector than in the dusk, which is further supported by the wave amplitudes derived from POES (Figures 9d and 9f). POES also revealed that the chorus amplitudes were strongest in the midnight MLT sector, but strong activity was also observed in the dawn and noon MLT sectors. The Van Allen Probes and POES both show that chorus activity started at higher L-shells and moved in to lower L during the main phase, and the peak in activity was centered around $L^* \sim 4$ between 00:00 and 09:00 UT on 1 October. After ~12:00 UT on 1 October, very little chorus activity was observed until around 11:00 and 18:00 UT on 2 October, corresponding to the energetic particle injections (Figure 8) and spikes in the AL index (Figure 1) observed around those same times.

4. Discussion

4.1. Event Summary and Conceptual Scenario

On 30 September 2012, CME activity in the solar wind buffeted Earth's magnetosphere, causing global geomagnetic activity that ultimately resulted in a strong geomagnetic storm, which lasted until 3 October. This storm's sudden commencement and main phase were associated with an intense flux dropout throughout the outer radiation belt, which was examined in detail by a companion paper [i.e., *Turner et al*., 2014]. This dropout eradicated the "storage ring" feature described by *Baker et al*. [2013], which itself formed after a different dropout in early September and may have been a remnant belt left over after the dropout [e.g., *Turner et al*., 2013]. The dropout on 30 September essentially wiped out the entire outer belt population, but a source of electrons started replenishing the belt during the main phase, counteracting the effects of the dropout. Despite this source of new electrons, the total content of the outer belt remained lower than the pre-storm level, revealing that losses dominated over sources during this storm.

We present the following scenario to explain the salient features of this storm as observed by 15 spacecraft and the CARISMA network of ground magnetometers. Competing source and loss mechanisms resulting from WPI were active in the heart of the outer radiation belt (i.e., $L^* < \sim 5$) during the main phase of this storm. At $L^* < 4$, EMIC waves in the dusk MLT sector caused sudden loss of >1 MeV electrons mirroring at high magnetic latitudes by scattering them into the atmospheric loss cone. Meanwhile, chorus waves locally accelerated electrons around $3.5 < L^* < 5$, evident as a growing peak in PSD. This acceleration affected electrons at all levels of μ and K examined, but its effect was strongest for lower-μ and near-equatorially mirroring electrons ($K \sim 0\,G^{1/2}R_E$). However, for higher μ and higher K (i.e., off-equatorially mirroring) electrons at $L^* < \sim 4$, the loss mechanism by EMIC WPI dominated over the source; this resulted in an overall depletion of electron PSD for $\mu > \sim 1200$ MeV/G (at all K) and $K > \sim 0.03\,G^{1/2}R_E$ (at all μ) over the full range of L-shells affected by the WPIs (see additional data in the supporting information). Furthermore, energetic particle injections from a source population in the plasma sheet likely played a key role in both of these processes by introducing the source (and seed) populations of 10–100 s of keV electrons that generated (and were simultaneously accelerated by) the chorus waves. Particle injections would also be responsible for introducing the energetic ions that could generate the EMIC waves near the plasmapause as they drifted through the dusk MLT sector. With this scenario in mind, we next revisit the evidence of WPI from the observations and compare them to expectations from quasi-linear theory.

4.2. Loss by WPI With EMIC Waves

To summarize the results of the analysis presented in section 3.1: The Van Allen Probes observed a sudden and strong loss of high-μ, high-K electrons between ~22:30 and ~03:00 UT at $L^* < 4$. For lower-μ, low-K electrons observed by both THEMIS and Van Allen Probes, this strong sudden loss was not evident. Between 22:50 and 01:00 UT, POES and SAMPEX observed very strong enhancements of >1 MeV electron fluxes at LEO; these enhancements were limited to L-shells < 4.5, which corresponded to $L^* < 4$, in the dusk MLT sector in both the northern and southern hemispheres. POES revealed a strong enhancement of the precipitating to trapped ratio of electrons and ring current ions (10 s to 100 s keV). SAMPEX did not observe a similar enhancement in the >500 keV population. THEMIS did not observe EMIC waves in the dusk MLT sector before or after the period of loss, and the Van Allen Probes did not observe EMIC waves in the dawn to pre-noon MLT sector during the period of loss. However, the CARISMA network of ground magnetometers observed EMIC waves between 22:00 and 01:30 UT; these EMIC waves were limited to $3 < L < 5$ and occurred in the dusk MLT sector between ~15:30 and 19:00 MLT. GOES-15 observed EMIC waves at GEO between 22:30 and 23:00 UT (not shown), but there were no enhancements in precipitating flux around these

L-shells, either due to a lack of MeV electrons here because of previous losses during the first part of the dropout or due to inadequate plasma density conditions for electron resonance.

Based on quasi-linear diffusion theory, EMIC waves should be most effective at scattering electrons at energies in the multi-MeV range and pitch angles closer to the atmospheric loss cone. Unfortunately, we cannot accurately model WPI between EMIC waves and relativistic electrons due to a lack of in situ observations of the waves during this event. With only ground observations of the EMIC waves, we are unable to estimate the electron resonant energy ranges and loss rates since we have no in situ detail of the EMIC wave spectrum, its proximity to the electron gyrofrequency, and plasma density. However, we can estimate the effects of WPIs between EMIC waves and relativistic electrons based on previous work. *Meredith et al*. [2003a] calculated minimum resonance energies for electrons interacting with EMIC waves based on observations from the CRRES mission. They found that the resonant energy was typically above 2 MeV, except in regions of high plasma density and/or weak magnetic field strength, where the ratio of the electron plasma frequency to equatorial electron cyclotron frequency was >10. Based on diffusion coefficients calculated by *Albert* [2003]; *Summers and Thorne* [2003], and *Shprits et al*. [2008b, 2013b], EMIC waves should cause rapid pitch angle scattering of electrons near the strong diffusion limit, which should result in rapid loss of electrons over a range of pitch angles within as little as 1 h. However, resonance also depends on the ion species present and those responsible for generating the EMIC waves [e.g., *Summers et al*., 2007; *Ukhorskiy et al*., 2010]. Furthermore, EMIC waves should only be effective at scattering electrons with equatorial pitch angles less than ~40–60° [*Thorne et al*., 2005; *Shprits et al*., 2008b]. The energy and pitch angle dependencies of electron scattering by EMIC waves are consistent with the recent observations of *Usanova et al*. [2014], who used Van Allen Probes data to examine the effects of EMIC waves on pitch angle distributions of electrons ranging in energy from 2 to 8 MeV. They found that the magnitude of electron losses increased with increasing energy (i.e., they were stronger at 8 MeV than at 2 MeV) and the losses were only effective over a limited range in equatorial pitch angle. Losses were strongest at equatorial pitch angles nearest the loss cone, with electrons at equatorial pitch angles around 90° being essentially unaffected by the loss. These results, both theoretical and observational, are consistent with the observations presented here from the 30 September to 3 October 2012 geomagnetic storm, supporting the scenario in which sudden loss of multi-MeV electrons mirroring at high latitudes occurred at $L^* < 4$ due to WPI with EMIC waves during the main phase of the storm.

4.3. Source by WPI With Chorus Waves

To summarize the results of the analysis presented in section 3.2: Growing peaks in relativistic electron PSD were observed by both THEMIS and Van Allen Probes over a broad range of μ and K. The enhancement was strongest at the lower μ's and higher K's examined (e.g., $\mu = 1000$ MeV/G, $K = 0.172\ G^{1/2}R_E$ shown in Figure 7). The PSD increased by factors between ~4 and >10 for different μ and K combinations in less than 10 h at $4 < L^* < 4.5$. The peaks in PSD stopped increasing after ~12:00 UT on 1 October. Throughout this storm, the L* distributions of electron PSD were peaked for all $\mu \geq 750$ MeV/G and $K < 0.02\ G^{1/2}R_E$ examined with THEMIS. This indicates that there was continually less relativistic electron PSD in the near-Earth plasma sheet than within the heart of the outer belt; thus, inward radial transport could not explain the observed enhancements in PSD since there was an insufficient source of relativistic electrons at higher L-shells or in the plasma sheet. Multiple energetic particle injections were observed by GOES, POES, THEMIS, and Van Allen Probes between 12:00 UT on 30 September and 12:00 UT on 1 October, and significant chorus wave activity was also observed (or indicated in the case of POES) by THEMIS, Van Allen Probes, and POES during this period.

Due to the multipoint observations of electron energy distributions and chorus wave activity throughout the system, we were able to use a two-dimensional energy and pitch angle diffusion model [*Ma et al*., 2012; *Thorne et al*., 2013b] to simulate the acceleration of electrons by WPI with chorus waves during this event. For the simulations, the period from 02:00 to 12:00 UT on 1 October was used with a 2 h time step at $L = 5.25$ (corresponding to an average L* of 4.5 during that period). Initial conditions for the electron PSD as a function of energy and pitch angle were taken from the Van Allen Probes data. Chorus amplitudes and distributions were taken from the POES and Van Allen Probes observations averaged over $4 \leq L \leq 6$. The plasma trough density model from *Sheeley et al*. [2001] was also employed, but we confirmed that the model density values were consistent with those observed by the Van Allen Probes around the dawn

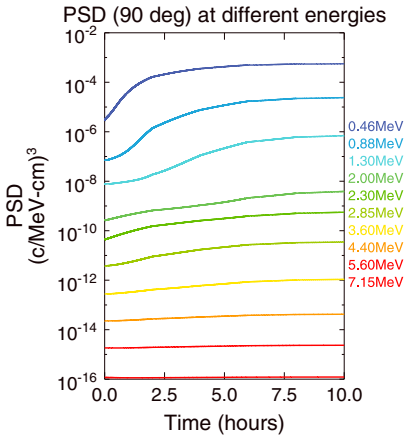

Figure 10. Two-dimensional momentum and pitch angle diffusion model results simulating the effects of chorus waves on relativistic electron distributions. This figure shows the evolution of the electron phase space density for electrons at various energies (from 460 keV to 7.15 MeV shown in different colors) and equatorial pitch angles of 90° at L = 5.25. For the simulation, time = 0 corresponds to 02:42 UT on 1 October. Model details are discussed in section 4.3 with additional details provided in the supporting information. For results at different equatorial pitch angles, see the supporting information.

sector. With those parameters, we were able to calculate pitch angle and energy diffusion coefficients and run the simulation.

The simulation results, an example from which is shown in Figure 10 for comparison (see also the plots of E and α_{eq} for different μ, K, and L-shells in the supporting information), are generally consistent with the observations from Van Allen probes. For example, electrons with $\mu = 2414$ MeV/G and $K = 0.015\ G^{1/2}R_E$ (see Figure 7) were enhanced by a factor of ~40 in 9 h at L* = 4.5 as observed by Van Allen Probes during the main and early recovery phases of this storm. The model showed that chorus waves around L* = 4.5 were able to enhance electrons at 2 MeV and equatorial pitch angles of 90° by a factor of ~20 over a 10 h period. For off-equatorially mirroring electrons, the Van Allen Probes observed a factor of ~8 increase for $\mu = 2414$ MeV/G, $K = 0.172\ G^{1/2}R_E$ electrons in ~9 h; the model also revealed a factor of 8 increase over 10 h for 2.85 MeV electrons with equatorial pitch angles ~30°. At lower energies (and μ), the enhancement was stronger; the Van Allen Probes observed a ~100 times increase in PSD for $\mu = 1000$ MeV/G and $K = 0.172\ G^{1/2}R_E$ electrons at L* = 4.5 over 12 h. This too is approximately consistent with the model, which revealed a factor of ~300 increase for 0.88 MeV electrons with equatorial pitch angles ~30°.

It is important to note that the simulations only considered interactions between chorus waves and energetic electrons using quasi-linear theory, and they were able to capture the levels and timescales of acceleration observed in this event. We also examined THEMIS and Van Allen Probes data for magnetosonic waves, since those waves may also play an important role in outer belt electron dynamics [e.g., *Horne and Thorne*, 1998]. However, none of those satellites observed strong magnetosonic wave activity in either the dawn or dusk sectors during the acceleration interval of 02–12 UT on 1 October. With the caveat that magnetosonic waves may have been more intense at other MLTs that were not directly observed, it is unlikely that magnetosonic waves played a significant role in the evolution of the relativistic electrons during this event based on the magnitude of the wave amplitudes that were observed by THEMIS and Van Allen Probes. This, along with the success of the simulations, provides additional evidence [see also *Thorne et al.*, 2013] suggesting that magnetosonic waves may not play an important role in relativistic electron acceleration [*Shprits et al.*, 2013a]. However, our comparison between the simulation results and observations also implies that some additional loss process (i.e., not from EMIC waves observed during the main phase at lower L-shells) may also have been ongoing during the enhancement and was more effective for lower energy (≤ ~1 MeV) electrons. Note that the energies and pitch angles listed here from the model correspond approximately to the corresponding μ and K from the observations to which we compared them. For additional detail, including the model results plus the Van Allen Probes observations over the full range of μ and K examined, please see the supporting information.

These results support the scenario in which local acceleration from WPI with whistler-mode chorus waves acted as a local source of ~ MeV electrons during the late main phase and early recovery phase of this storm. This source was only active until ~12:00 UT on 1 October, at which point the peaks in electron PSD stopped growing and afterward only slow decay was observed. The timing of the acceleration corresponded to the most active period of substorm activity (see the AE and AL indices in Figure 1d), energetic particle injections (see Figure 8), and chorus waves (see Figure 9). This picture is entirely consistent with the theory and previous observations of relativistic electron acceleration by WPI with chorus [e.g., *Horne and Thorne*, 1998; *Summers et al.*, 1998; *Horne et al.*, 2005; *Chen et al.*, 2007; *Turner and Li*, 2008; *Turner et al.*, 2010; *Turner et al.*, 2012c; *Reeves et al.*, 2013; *Thorne et al.*, 2013b; A. Boyd et al., Quantifying the radiation belt seed population in the March 17, 2013 electron

acceleration event, submitted to *Geophysical Research Letters*, 2013]. In this picture of the system, a seed population of 10 s to 100 s of keV electrons, whose source is in the near-Earth plasma sheet, is introduced to the inner magnetosphere during periods of enhanced convection and/or energetic particle injections. Electrons at lower energies can serve as the source population for chorus waves. When the chorus waves interact with the seed population of electrons, they can be accelerated to relativistic electrons, resulting in growing peaks in PSD that can increase by more than two orders of magnitude in only ~12 h.

5. Conclusions

The multipoint observations presented here provide observational evidence of competing WPI driving losses and sources that alter the balance of relativistic electrons in the outer belt during the late main phase of the large geomagnetic storm that started on 30 September 2012. First, these observations are additional direct observational evidence [see also *Miyoshi et al*., 2008; *Usanova et al*., 2014] that loss of relativistic electrons from the outer belts via WPI with EMIC waves does occur and can contribute to rapid loss during dropout events. As expected from theory, the plasmapause apparently played a critical role in the WPI, since the interactions occurred along or just outside of it, and only electrons at very high energy (several MeV; high-μ) and mirroring at high latitudes (equatorial pitch angles away from 90°; high-K) were affected by the loss. Thus, losses from WPI with EMIC waves may explain dropouts of multi-MeV electrons that are not associated with magnetopause shadowing [e.g., *Shprits et al*., 2012] or that extend to lower L-shells than can be affected by magnetopause shadowing and subsequent outward radial diffusion [e.g., *Bortnik et al*., 2006], as was also the case here [see additional details in *Turner et al*., 2014].

Our results also provide direct observational evidence of local acceleration of relativistic outer belt electrons by WPI with chorus waves. The acceleration was effective over a range of electron energies, from 100 s of keV to $>$5 MeV and a range of equatorial pitch angles, but the enhancements were strongest for lower energies (100 s of keV to ~1 MeV) and equatorial pitch angles near 90°. The results also indicated how energetic particle injections during periods of substorm activity and the plasmapause play an important role in relativistic electron acceleration by WPI with chorus waves: the acceleration occurred outside of the plasmapause and ceased after the IMF turned northward, coinciding with the cessation of substorm activity, electron injections, and chorus waves. The observed PSD enhancements agreed well with simulations using a two-dimensional, energy and pitch angle diffusion model with the observed chorus distributions and intensities at $L^* = 4.5$. However, the comparison between the observations and the simulation results also indicated that some other loss mechanism may have been in effect after the EMIC waves subsided, since the enhancement of lower-energy ($\leq$ ~1 MeV) electrons was not as strong as that in the simulations. We suspect that, since the plasmapause remained inside of $L = 3.3$ during the acceleration period [*Turner et al*., 2014], the additional loss was probably not due to plasmaspheric hiss, which is an energy-dependent loss mechanism that is more effective for lower-energy relativistic electrons [e.g., *Thorne et al*., 2013a; *Shprits et al*., 2013b]. Loss may have occurred due to interactions with chorus waves at higher latitudes on the dayside [*Li et al*., 2007] or outward radial transport away from the peak in PSD. Another possibility to explain the additional loss is by nonlinear WPI with large-amplitude chorus waves [e.g., *Albert*, 2002; *Bortnik et al*., 2008; *Catell et al*., 2008; *Santolik et al*., 2014; *Tao et al*., 2012], though there are many outstanding questions concerning the nature of such interactions.

Finally, concerning the competitive nature of the interactions, between ~23:00 UT on 30 September and ~05:00 UT on 1 October, both EMIC waves and chorus waves were affecting the intensity of relativistic electrons, which provided us an interesting opportunity to study the competitive nature of these WPI. When both types of waves were active, WPI with chorus resulted in a local source of relativistic electrons between $\sim 3.5 < L^* < \sim 5.5$, while the losses were restricted to $L^* < \sim 4$, so the two mechanisms were competing in the range $3.5 < L^* < 4$. Based on the multipoint PSD results from THEMIS and Van Allen Probes (Figures 2, 3, and 7 and supporting information) in this L* range, the source dominated over loss at lower energies (corresponding to $\mu < \sim 1200$ MeV/G) and near-equatorially mirroring electrons ($K < \sim 0.03\, G^{1/2} R_E$), but losses to the atmosphere dominated over sources for higher energy electrons and those mirroring at high latitudes. Ultimately, however, the chorus waves were longer lived than the EMIC waves, and local acceleration continued after the EMIC waves subsided. Despite this, the combined losses due to magnetopause shadowing at $L^* > \sim 4$ and EMIC waves at $L^* < \sim 4$ during the main phase of this strong storm were more intense than the local

source during the late main phase and early recovery phase, since this storm ultimately resulted in an outer belt depletion compared to pre-storm levels. These results represent just one storm, and observations from 15 spacecraft and ground observatories were necessary to shed light on the nature and complexity of the competing source and loss mechanisms. Future statistical studies of multiple storm and/or non-storm events should account for this complexity and characterize the parameters important to each of the different source and loss mechanisms, including the WPI highlighted here, when trying to relate various solar wind drivers and indicators of magnetospheric activity to responses of relativistic electrons in the outer radiation belt.

Acknowledgments

We are thankful to the THEMIS and Van Allen Probes missions, NASA's CDAWeb, OMNI, and NOAA's GOES and NGDC for online data access and data analysis tools. RBSP-ECT work was supported under NASA prime contract NAS5-01072 to Johns Hopkins University Applied Physics Laboratory (JHU/APL). Work at LANL was performed under the auspices of the United States Department of Energy. D. L. Turner is thankful for funding from NASA's THEMIS mission (contract NAS5-02099), a NASA grant (NNX12AJ55G), and the Monitoring, Analyzing, and Assessing the Radiation Belt Loss and Energization (MAARBLE) project funded under the European Commission's (EC) FP7 framework (Note that this work reflects the authors' views, and the EC is not liable for any use that may be made of the information contained herein).

Michael Liemohn thanks Xin Tao and an anonymous reviewer for their assistance in evaluating this paper.

References

Albert, J. M. (2002), Nonlinear interaction of outer zone electrons with VLF waves, *Geophys. Res. Lett.*, *29*(8), 1275, doi:10.1029/2001GL013941.

Albert, J. M. (2003), Evaluation of quasi-linear diffusion coefficients for EMIC waves in a multispecies plasma, *J. Geophys. Res.*, *108*(A6), 1249, doi:10.1029/2002JA009792.

Anderson, B. J., R. E. Erlandson, and L. J. Zanetti (1992), A statistical study of Pc 1–2 magnetic pulsations in the equatorial magnetosphere: 2. Wave properties, *J. Geophys. Res.*, *97*, 3089–3101.

Angelopoulos, V. (2008), The THEMIS Mission, *Space Sci. Rev.*, *141*, 5–34, doi:10.1007/s11214-008-9336-1.

Auster, H. U., et al. (2008), The THEMIS fluxgate magnetometer, *Space Sci. Rev.*, *141*, 235–264, doi:10.1007/s11214-008-9365-9.

Baker, D. N., et al. (1998), A strong CME-related magnetic cloud interaction with the Earth's magnetosphere: ISTP observations of rapid relativistic electron acceleration on May 15, 1997, *Geophys. Res. Lett.*, *25*, 2975–2978.

Baker, D. N., G. M. Mason, O. Figueroa, G. Colon, J. G. Watzin, and R. M. Aleman (1993), An overview of the Solar, Anomalous, and Magnetospheric Particle Explorer (SAMPEX) mission, *IEEE Trans. Geosci. Remote Sens.*, *31*, 532–541, doi:10.1109/26.225519.

Baker, D. N., et al. (2012), The Relativistic Electron-Proton Telescope (REPT) instrument on board the Radiation Belt Storm Probes (RBSP) spacecraft: Characterization of Earth's radiation belt high-energy particle populations, *Space Sci. Rev.*, doi:10.1007/s11214-012-9950-9.

Baker, D. N., et al. (2013), A long-lived relativistic electron storage ring embedded in Earth's outer Van Allen belt, *Science*, *340*, doi:10.1126/science.1233518.

Blake, J. B., et al. (2013), The Magnetic Electron Ion Spectrometer (MagEIS) instruments aboard the Radiation Belt Storm Probes (RBSP) spacecraft, *Space Sci. Rev.*, doi:10.1007/s11214-013-9991-8.

Borovsky, J. E., and M. H. Denton (2009), Relativistic-electron dropouts and recovery: A superposed epoch study of the magnetosphere and the solar wind, *J. Geophys. Res.*, *114*, A02201, doi:10.1029/2008JA013128.

Bortnik, J., R. M. Thorne, T. P. O'Brien, J. C. Green, R. J. Strangeway, Y. Y. Shprits, and D. N. Baker (2006), Observation of two distinct, rapid loss mechanisms during the 20 November 2003 radiation belt dropout event, *J. Geophys. Res.*, *111*, A12216, doi:10.1029/2006JA011802.

Bortnik, J., R. M. Thorne, and U. S. Inan (2008), Nonlinear interaction of energetic electrons with large amplitude chorus, *Geophys. Res. Lett.*, *35*, L21102, doi:10.1029/2008GL035500.

Cattell, C., et al. (2008), Discovery of very large amplitude whistler-mode waves in Earth's radiation belts, *Geophys. Res. Lett.*, *35*, L01105, doi:10.1029/2007GL032009.

Chen, Y., et al. (2007), The energization of relativistic electrons in the outer Van Allen radiation belt, *Nat. Phys.*, *3*, 614–617.

Cornwall, J. M. (1965), Cyclotron instabilities and electromagnetic emission in the ultra low frequency and very low frequency ranges, *J. Geophys. Res.*, *70*(1), 61–69.

Cully, C. M., R. E. Ergun, K. Stevens, A. Nammari, and J. Westfall (2008), The THEMIS Digital Fields Board, *Space Sci. Rev.*, *141*, doi:10.1007/s11214-008-9417-1.

Elkington, S. R., M. K. Hudson, and A. A. Chan (2003), Resonant acceleration and diffusion of outer zone electrons in an asymmetric geomagnetic field, *J. Geophys. Res.*, *108*(A3), 1116, doi:10.1029/2001JA009202.

Evans, D. S., and M. S. Greer (2004), Polar Operational Environment Satellite Space Environment Monitor-2: Instrument descriptions and archive data documentation, *NOAA Tech. Mem.*, *93*, 47, version 1.4.

Fraser, B. J., and T. S. Nguyen (2001), Is the plasmapause a preferred source region of electromagnetic ion cyclotron waves in the magnetosphere?, *J. Atmos. Sol. Terr. Phys.*, *63*(11), 1225–1247.

Fraser, B. J., H. J. Singer, M. L. Adrian, D. L. Gallagher, and M. F. Thomsen (2005), The relationship between plasma density structure and emic waves at geosynchronous orbit, in *Inner Magnetosphere Interactions: New Perspectives from Imaging, Geophys. Monogr. Ser.*, vol. 159, edited by J. Burch, M. Schulz, and H. Spence, pp. 55–70, AGU, Washington, D. C., doi:10.1029/159GM04.

Friedel, R. H. W., G. D. Reeves, and T. Obara (2002), Relativistic electron dynamics in the inner magnetosphere – a review, *J. Atmos. Sol. Terr. Phys.*, *64*, 265–682.

Gary, S. P., and M. A. Lee (1994), The ion cyclotron anisotropy instability and the inverse correlation between proton anisotropy and proton beta, *J. Geophys. Res.*, *99*(A6), 11,297–11,301, doi:10.1029/94JA00253.

Gendrin, R. (1975), Is the plasmapause a preferential region for proton precipitation?, *Ann. Geophys.*, *31*, 127–136.

Goldstein, J., B. R. Sandel, M. F. Thomsen, M. Spasojevic´, and P. H. Reiff (2004), Simultaneous remote sensing and in situ observations of plasmaspheric drainage plumes, *J. Geophys. Res.*, *109*, A03202, doi:10.1029/2003JA010281.

Gonzalez, W. D., B. T. Tsurutani, and A. L. Clua de Gonzalez (1999), Interplanetary origin of geomagnetic storms, *Space Sci. Rev.*, *88*, 529–562.

Green, J. C., and M. G. Kivelson (2004), Relativistic electrons in the outer radiation belt: Differentiating between acceleration mechanisms, *J. Geophys. Res.*, *109*, A03213, doi:10.1029/2003JA010153.

Horne, R. B., and R. M. Thorne (1998), Potential waves for relativistic electron scattering and stochastic acceleration during magnetic storms, *Geophys. Res. Lett.*, *25*(15), 3011–3014.

Horne, R. B., R. M. Thorne, S. A. Glauert, J. M. Albert, N. P. Meredith, and R. R. Anderson (2005), Timescale for radiation belt electron acceleration by whistler mode chorus waves, *J. Geophys. Res.*, *110*, A03225, doi:10.1029/2004JA010811.

Hudson, M. K., S. R. Elkington, J. G. Lyon, and C. C. Goodrich (2000), Increase in relativistic electron flux in the inner magnetosphere: ULF wave mode structure, *Adv. Space Res.*, *25*, 2327–2337.

Hudson, M. K., D. N. Baker, J. Goldstein, B. Kress, J. Paral, F. Toffoletto, and M. Wiltberger (2014), Simulated magnetopause losses and Van Allen Probe flux dropouts, *Geophys. Res. Lett.*, doi:10.1002/2014GL059222, in press.

Hwang, J., D.-Y. Lee, K.-C. Kim, D.-K. Shin, J.-H. Kim, J.-H. Cho, M.-Y. Park, and D. L. Turner (2013), Significant loss of energetic electrons at the heart of the outer radiation belt during weak magnetic storms, *J. Geophys. Res. Space Physics*, *118*, 4221–4236, doi:10.1002/jgra.50410.

Kim, K. C., D.-Y. Lee, H.-J. Kim, L. R. Lyons, E. S. Lee, M. K. Ozturk, and C. R. Choi (2008), Numerical calculations of relativistic electron drift loss effect, *J. Geophys. Res.*, *113*, A09212, doi:10.1029/2007JA013011.

Kim, K.-C., D.-Y. Lee, Y. Shprits, H.-J. Kim, and E. Lee (2011), Electron flux changes in the outer radiation belt by radial diffusion during the storm recovery phase in comparison with the fully adiabatic evolution, *J. Geophys. Res.*, *116*, A09229, doi:10.1029/2011JA016642.

Klecker, B., et al. (1993), HILT: A heavy ion large area proportional counter telescope for solar and anomalous cosmic rays, *IEEE Trans. Geosci. Remote Sens.*, *31*(3), 542–548.

Kletzing, C. A., et al. (2013), The Electric and Magnetic Field Instrument Suite and Integrated Science (EMFISIS) on RBSP, *Space Sci. Rev.*, doi:10.1007/s11214-013-9993-6.

Kozyra, J. U., T. E. Cravens, F. Nagy, and E. G. Fontheim (1984), Effects of energetic heavy ions on electromagnetic ion cyclotron wave generation in the plasmapause region, *J. Geophys. Res.*, *89*(A4), 2217–2233, doi:10.1029/JA089iA04p02217.

Lam, M. M., R. B. Horne, N. P. Meredith, S. A. Glauert, T. Moffat-Griffin, and J. C. Green (2010), Origin of energetic electron precipitation >30 keV into the atmosphere, *J. Geophys. Res.*, *115*, A00F08, doi:10.1029/2009JA014619.

Li, W., Y. Y. Shprits, and R. M. Thorne (2007), Dynamic evolution of energetic outer zone electrons due to wave-particle interactions during storms, *J. Geophys. Res.*, *112*, A10220, doi:10.1029/2007JA012368.

Li, W., R. M. Thorne, V. Angelopoulos, J. Bortnik, C. M. Cully, B. Ni, O. LeContel, A. Roux, U. Auster, and W. Magnes (2009), Global distribution of whistler-mode chorus waves observed on the THEMIS spacecraft, *Geophys. Res. Lett.*, *36*, L09104, doi:10.1029/2009GL037595.

Li, W., J. Bortnik, R. M. Thorne, and V. Angelopoulos (2011), Global distribution of wave amplitudes and wave normal angles of chorus waves using THEMIS wave observations, *J. Geophys. Res.*, *116*, A12205, doi:10.1029/2011JA017035.

Li, W., B. Ni, R. M. Thorne, J. Bortnik, J. C. Green, C. A. Kletzing, W. S. Kurth, and G. B. Hospodarsky (2013), Constructing the global distribution of chorus wave intensity using measurements of electrons by the POES satellites and waves by the Van Allen Probes, *Geophys. Res. Lett.*, *40*, 4526–4532, doi:10.1002/grl.50920.

Lin, R. L., X. X. Zhang, S. Q. Liu, Y. L. Wang, and J. C. Gong (2010), A three-dimensional asymmetric magnetopause model, *J. Geophys. Res.*, *115*, A04207, doi:10.1029/2009JA014235.

Loto'aniu, T. M., H. J. Singer, C. L. Waters, V. Angelopoulos, I. R. Mann, S. R. Elkington, and J. W. Bonnell (2010), Relativistic electron loss due to ultralow frequency waves and enhanced outward radial diffusion, *J. Geophys. Res.*, *115*, A12245, doi:10.1029/2010JA015755.

Lyons, L. R., and R. M. Thorne (1973), Equilibrium structure of radiation belt electrons, *J. Geophys. Res.*, *78*(13), 2142–2149.

Ma, Q., B. Ni, X. Tao, and R. M. Thorne (2012), Evolution of the plasma sheet electron pitch angle distribution by whistler-mode chorus waves in non-dipole magnetic fields, *Ann. Geophys.*, *30*, 751–760, doi:10.5194/angeo-30-751-2012.

Manchester, R. N. (1966), Propagation of Pc 1 micropulsations from high to low latitudes, *J. Geophys. Res.*, *71*(15), 3749–3754, doi:10.1029/JZ071i015p03749.

Mann, I. R., et al. (2008), The updated CARISMA magnetometer array in the THEMIS Era, *Space Sci. Rev.*, *141*, 413–451.

Mann, I. R., K. R. Murphy, L. G. Ozeke, I. J. Rae, D. K. Milling, A. Kale, and F. Honary (2012), The role of ultralow frequency waves in radiation belt dynamics, in *Dynamics of the Earth's Radiation Belts and Inner Magnetosphere*, *Geophys. Monogr. Ser.*, vol. 199, edited by D. Summers et al., pp. 69–91, AGU, Washington, D. C., doi:10.1029/2012GM001349.

Mann, I. R., et al. (2014), Spatial localization and ducting of EMIC waves: Van Allen Probes and ground-based observations, *Geophys. Res. Lett.*, doi:10.1002/2013GL058581, in press.

Mason, G. M., D. C. Hamilton, P. H. Walpole, K. F. Heuerman, T. L. James, M. H. Lennard, and J. E. Mazur (1993), LEICA: A low energy ion composition analyzer for the study of solar and magnetospheric heavy ions, *IEEE Trans. Geosci. Rem. Sens.*, *31*(3), 549–556.

Matsumura, C., Y. Miyoshi, K. Seki, S. Saito, V. Angelopoulos, and J. Koller (2011), Outer radiation belt boundary location relative to the magnetopause: Implications for magnetopause shadowing, *J. Geophys. Res.*, *116*, A06212, doi:10.1029/2011JA016575.

Meredith, N. P., R. B. Horne, and R. R. Anderson (2001), Substorm dependence of chorus amplitudes: Implications for the acceleration of electrons to relativistic energies, *J. Geophys. Res.*, *106*(A7), 13,165–13,178, doi:10.1029/2000JA900156.

Meredith, N. P., R. M. Thorne, R. B. Horne, D. Summers, B. J. Fraser, and R. R. Anderson (2003a), Statistical analysis of relativistic electron energies for cyclotron resonance with EMIC waves observed on CRRES, *J. Geophys. Res.*, *108*(A6), 1250, doi:10.1029/2002JA009700.

Meredith, N. P., R. B. Horne, R. M. Thorne, and R. R. Anderson (2003b), Favored regions for chorus-driven electron acceleration to relativistic energies in the Earth's outer radiation belt, *Geophys. Res. Lett.*, *30*(16), 1871, doi:10.1029/2003GL017698.

Millan, R. M., and R. M. Thorne (2007), Review of radiation belt relativistic electron losses, *J. Atmos. Sol. Terr. Phys.*, *69*, doi:10.1016/j.jastp.2006.06.019.

Miyoshi, Y., A. Morioka, T. Obara, H. Misawa, T. Nagai, and Y. Kasahara (2003), Rebuilding process of the outer radiation belt during the 3 November 1993 magnetic storm: NOAA and Exos-D observations, *J. Geophys. Res.*, *108*(A1), 1004, doi:10.1029/2001JA007542.

Miyoshi, Y., K. Sakaguchi, K. Shiokawa, D. Evans, J. Albert, M. Connors, and V. Jordanova (2008), Precipitation of radiation belt electrons by EMIC waves, observed from ground and space, *Geophys. Res. Lett.*, *35*, L23101, doi:10.1029/2008GL035727.

Morley, S. K., S. T. Ables, M. D. Sciffer, and B. J. Fraser (2009), Multipoint observations of Pc1-2 waves in the afternoon sector, *J. Geophys. Res.*, *114*, A09205, doi:10.1029/2009JA014162.

Morley, S. K., et al. (2010), Dropouts of the outer electron radiation belt in response to solar wind stream interfaces: Global positioning system observations, *Proc. Roy. Soc. A*, *466*, 3329–3350.

Morley, S. K., M. G. Henderson, G. D. Reeves, R. H. W. Friedel, and D. N. Baker (2013), Phase Space Density matching of relativistic electrons using the Van Allen Probes: REPT results, *Geophys. Res. Lett.*, *40*, 4798–4802, doi:10.1002/grl.50909.

Neudegg, D. A., B. J. Fraser, F. W. Menk, H. J. Hansen, G. B. Burns, R. J. Morris, and M. J. Underwood (1995), Sources and veolcities of Pc1-2 ULF waves at high-latitudes, *Geophys. Res. Lett.*, *22*(21), 2965–2968.

Ni, B., Y. Y. Shprits, R. H. W. Friedel, R. M. Thorne, M. Daae, and Y. Chen (2013), Responses of Earth's radiation belts to solar wind dynamic pressure variations in 2002 analyzed using multisatellite data and Kalman filtering, *J. Geophys. Res. Space Physics*, *118*, 4400–4414, doi:10.1002/jgra.50437.

Reeves, G. D., R. H. W. Friedel, R. D. Belian, M. M. Meier, M. G. Henderson, T. Onsager, H. J. Singer, D. N. Baker, X. Li, and J. B. Blake (1998), The relativistic electron response at geosynchronous orbit during the January 1997 magnetic storm, *J. Geophys. Res.*, *103*(A8), 17,559–17,570.

Reeves, G. D., K. L. McAdams, R. H. W. Friedel, and T. P. O'Brien (2003), Acceleration and loss of relativistic electrons during geomagnetic storms, *Geophys. Res. Lett.*, *30*(10), 1529, doi:10.1029/2002GL016513.

Reeves, G. D., et al. (2013), Electron acceleration in the heart of the Van Allen radiation belts, *Science*, *341*(6149), 991–994, doi:10.1126/science.1237743.

Rodger, C. J., M. A. Clilverd, J. C. Green, and M. M. Lam (2010), Use of POES SEM-2 observations to examine radiation belt dynamics and energetic electron precipitation into the atmosphere, *J. Geophys. Res.*, *115*, A04202, doi:10.1029/2008JA014023.

Roederer, J. G. (1970), *Dynamics of Geomagnetically Trapped Radiation*, pp. 166, Springer, New York.
Santolik, O., D. A. Gurnett, J. S. Pickett, M. Parrot, and N. Cornilleau-Wehrlin (2003), Spatio-temporal structure of storm-time chorus, *J. Geophys. Res.*, *108*(A7), 1278, doi:10.1029/2002JA009791.
Santolík, O., C. A. Kletzing, W. S. Kurth, G. B. Hospodarsky, and S. R. Bounds (2014), Fine structure of large-amplitude chorus wave packets, *Geophys. Res. Lett.*, *41*, 293–299, doi:10.1002/2013GL058889.
Schulz, M., and L. J. Lanzerotti (1974), *Particle Diffusion in the Radiation Belts*, Springer, New York.
Sheeley, B. W., M. B. Moldwin, H. K. Rassoul, and R. R. Anderson (2001), An empirical plasmasphere and trough density model: CRRES observations, *J. Geophys. Res.*, *106*(A11), 25,631–25,641, doi:10.1029/2000JA000286.
Shprits, Y. Y., R. M. Thorne, R. H. W. Friedel, G. D. Reeves, J. Fennell, D. N. Baker, and S. G. Kanekal (2006), Radial diffusion driven by losses at magnetopause, *J. Geophys. Res.*, *111*, A11214, doi:10.1029/2006JA011657.
Shprits, Y. Y., S. R. Elkington, N. P. Meredith, and D. Subbotin (2008a), Review of modeling losses and sources of relativistic electrons in the outer radiation belt I: Radial transport, *J. Atmos. Sol. Terr. Phys.*, *70*, doi:10.1016/j.jastp.2008.06.008.
Shprits, Y. Y., D. Subbotin, N. P. Meredith, and S. R. Elkington (2008b), Review of modeling of losses and sources of relativistic electrons in the outer radiation belt II: Local acceleration and loss, *J. Atmos. Sol. Terr. Phys.*, *70*, doi:10.1016/j.jastp.2008.06.014.
Shprits, Y. Y., M. Daae, and B. Ni (2012), Statistical analysis of phase space density buildups and dropouts, *J. Geophys. Res.*, *117*, A01219, doi:10.1029/2011JA016939.
Shprits, Y. Y., A. Runov, and B. Ni (2013a), Gyro-resonant scattering of radiation belt electrons during the solar minimum by fast magnetosonic waves, *J. Geophys. Res. Space Physics*, *118*, 648–652, doi:10.1002/jgra.50108.
Shprits, Y. Y., D. Subbotin, A. Drozdov, M. E. Usanova, A. Kellerman, K. Orlova, D. N. Baker, D. L. Turner, and K.-C. Kim (2013b), Unusual stable trapping of ultrarelativistic electrons in the Van Allen radiation belts, *Nat. Phys.*, *9*, doi:10.1038/NPHYS2760.
Spence, H. E., et al. (2013), Science goals and overview of the Energetic particle, Composition, and Thermal plasma (ECT) suite on NASA's Radiation Belt Storm Probes (RBSP) mission, *Space Sci. Rev.*, doi:10.1007/s11214-013-0007-5.
Summers, D., R. M. Thorne, and F. Xiao (1998), Relativistic theory of wave-particle resonant diffusion with application to electron acceleration in the magnetosphere, *J. Geophys. Res.*, *103*(A9), 20,487–20,500.
Summers, D., and R. M. Thorne (2003), Relativistic electron pitch-angle scattering by electromagnetic ion cyclotron waves during geomagnetic storms, *J. Geophys. Res.*, *108*(A4), 1143, doi:10.1029/2002JA009489.
Summers, D., B. Ni, and N. P. Meredith (2007), Timescales for radiation belt electron acceleration and loss due to resonant wave-particle interactions: 2. Evaluation for VLF chorus, ELF hiss, and electromagnetic ion cyclotron waves, *J. Geophys. Res.*, *112*, A04207, doi:10.1029/2006JA011993.
Tao, X., J. Bortnik, R. M. Thorne, J. M. Albert, and W. Li (2012), Effects of amplitude modulation on nonlinear interactions between electrons and chorus waves, *Geophys. Res. Lett.*, *39*, L06102, doi:10.1029/2012GL051202.
Temerin, M., I. Roth, M. K. Hudson, and J. R. Wygant (1994), New paradigm for the transport and energization of radiation belt particles, *Eos Trans. AGU*, *75*(44), *Fall Meet.*, Suppl., 538.
Thorne, R. M., and C. F. Kennel (1971), Relativistic electron precipitation during magnetic storm main phase, *J. Geophys. Res.*, *76*(19), 4446–4453.
Thorne, R. M., T. P. O'Brien, Y. Y. Shprits, D. Summers, and R. B. Horne (2005), Timescale for MeV electron microburst loss during geomagnetic storms, *J. Geophys. Res.*, *110*A09202, doi:10.1029/2004JA010882.
Thorne, R. M., R. B. Horne, V. K. Jordanova, J. Bortnik, and S. Glauer (2006), Interaction of EMIC waves with thermal plasma and radiation belt particles, in *Magnetospheric ULF Waves: Synthesis and New Directions*, *Geophys. Monogr. Ser.*, vol. 169, edited by K. Takahashi et al., pp. 213–223, AGU, Washington, D. C., doi:10.1029/169GM14.
Thorne, R. M. (2010), Radiation belt dynamics: The importance of wave-particle interactions, *Geophys. Res. Lett.*, *37*, L22107, doi:10.1029/2010GL044990.
Thorne, R. M., et al. (2013a), Evolution and slow decay of an unusual narrow ring of relativistic electrons near L ~ 3.2 following the September 2012 magnetic storm, *Geophys. Res. Lett.*, *40*, 3507–3511, doi:10.1002/grl.50627.
Thorne, R. M., et al. (2013b), Rapid acceleration of relativistic radiation belt electrons by magnetospheric chorus, *Nature*, *504*, 411–414, doi:10.1038/nature12889.
Tsurutani, B. T., and E. J. Smith (1974), Postmidnight chorus: A substorm phenomenon, *J. Geophys. Res.*, *79*(1), 118–127.
Tsyganenko, N. A., and M. I. Sitnov (2005), Modeling the dynamics of the inner magnetosphere during strong geomagnetic storms, *J. Geophys. Res.*, *110*, A03208, doi:10.1029/2004JA010798.
Turner, D. L., and X. Li (2008), Radial gradients of phase space density of the outer radiation belt electrons prior to sudden solar wind pressure enhancements, *Geophys. Res. Lett.*, *35*, L18101, doi:10.1029/2008GL034866.
Turner, D. L., X. Li, G. D. Reeves, and H. J. Singer (2010), On phase space density radial gradients of Earth's outer-belt electrons prior to sudden solar wind pressure enhancements: Results from distinctive events and a superposed epoch analysis, *J. Geophys. Res.*, *115*, A01205, doi:10.1029/2009JA014423.
Turner, D. L., S. Morley, Y. Miyoshi, B. Ni, and C.-L. Huang (2012a), Outer radiation belt flux dropouts: Current understanding and unresolved questions, in *Dynamics of Earth's Radiation Belts and Inner Magnetosphere*, *Geophys. Monogr. Ser.*, vol. 199, edited by D. Summers et al., pp. 195-212, AGU, Washington, D. C., doi:10.1029/2012GM001310.
Turner, D. L., Y. Y. Shprits, M. Hartinger, and V. Angelopoulos (2012b), Explaining sudden losses of relativistic electrons during geomagnetic storms, *Nature Phys.*, *8*, doi:10.1038/NPHYS2185.
Turner, D. L., V. Angelopoulos, Y. Shprits, A. Kellerman, P. Cruce, and D. Larson (2012c), Radial distributions of equatorial phase space density for outer radiation belt electrons, *Geophys. Res. Lett.*, *39*, L09101, doi:10.1029/2012GL051722.
Turner, D. L., V. Angelopoulos, W. Li, M. D. Hartinger, M. Usanova, I. R. Mann, J. Bortnik, and Y. Shprits (2013), On the storm-time evolution of relativistic electron phase space density in Earth's outer radiation belt, *J. Geophys. Res. Space Physics*, *118*, 2196–2212, doi:10.1002/jgra.50151.
Turner, D. L., et al. (2014), On the cause and extent of outer radiation belt losses during the 30 September 2012 dropout event, *J. Geophys. Res. Space Physics*, *119*, doi:10.1002/2013JA019446.
Ukhorskiy, A. Y., M. I. Sitnov, K. Takahashi, and B. J. Anderson (2009), Radial transport of radiation belt electron due to stormtime Pc5 waves, *Ann. Geophys.*, *27*, 2173–2181.
Ukhorskiy, A. Y., Y. Y. Shprits, B. J. Anderson, K. Takahashi, and R. M. Thorne (2010), Rapid scattering of radiation belt electrons by storm-time EMIC waves, *Geophys. Res. Lett.*, *37*, L09101, doi:10.1029/2010GL042906.
Usanova, M. E., I. R. Mann, J. Bortnik, L. Shao, and V. Angelopoulos (2012), THEMIS observations of electromagnetic ion cyclotron wave occurrence: Dependence on AE, SYMH, and solar wind dynamic pressure, *J. Geophys. Res.*, *117*, A10218, doi:10.1029/2012JA018049.

Usanova, M. E., F. Darrouzet, I. R. Mann, and J. Bortnik (2013), Statistical analysis of EMIC waves in plasmaspheric plumes from Cluster observations, *J. Geophys. Res. Space Physics*, *118*, 4946–4951, doi:10.1002/jgra.50464.

Usanova, M. E., et al. (2014), Effect of EMIC waves on relativistic and ultra-relativistic electron populations: Ground-based and Van Allen Probes Observations, *Geophys. Res. Lett.*, doi:10.1002/2013GL059024.

Zhao, H., and X. Li (2013), Inward shift of outer radiation belt electrons as a function of Dst index and the influence of the solar wind on electron injections into the slot region, *J. Geophys. Res. Space Physics*, *118*, 756–764, doi:10.1029/2012JA018179.